Available online at www.sciencedirect.com

ScienceDirect

Underground Space 27 (2026) 112–131

www.keaipublishing.com/undsp

Research Paper

# Modified linear superposition method for stress tensor field analysis and its application to compressed air energy storage chamber group

Zeyuan Sun [a], Cheng Zhao [a,b,*], Qinyuan Luo [a], Ran Huang [a], Ning Jia [c], Jinquan Xing [a,b], Jialun Niu [a,b], Chao Wei [a]

[a] *Department of Geotechnical Engineering, College of Civil Engineering, Tongji University, Shanghai 200092, China*
[b] *Key Laboratory of Geotechnical and Underground Engineering of Ministry of Education, Tongji University, Shanghai 200092, China*
[c] *North China Power Engineering Co., Ltd. of China Power Engineering Consulting Group, Beijing 100120, China*

Received 28 November 2024; received in revised form 9 February 2025; accepted 21 March 2025
Available online 05 January 2026

**Abstract**

Burial depth and spacing are key factors influencing the stability of compressed air energy storage chamber groups. However, methods for determining safe burial depth and spacing in aligned multi-chamber systems remain underexplored. This study introduces a modified linear superposition method (M-LSM) for calculating elastic stress tensor fields in the surrounding rock around multiple chambers. The method analyzes the distribution of elastic stress under varying design parameters and surrounding rock conditions, identifying the most critical stress locations, which are the sidewalls affected by adjacent chambers, and providing deeper insights into stress concentrations caused by chamber interactions. The relationship between safe burial depth and spacing follows an approximately inverse proportionality, with the safety criterion of no plastic zones developing in the surrounding rock. A closed-form solution for safe burial depth and spacing is derived, which can be used to quickly determine the design parameters. The M-LSM is applicable to a wide range of internal pressurized chamber groups and borehole problems, capturing mutual interactions between adjacent chambers more realistically. Compared to finite element method simulations based on a practical engineering case, the results show errors that are typically negligible, validating the reliability of the analytical approach. This fully analytical method is mesh-free, iteration-free, and offers infinite resolution, making it highly efficient for both computations and practical applications. The closed-form solution derived from this method provides significant value for trend analysis, practical calculations, and engineering applications.

*Keywords:* Linear superposition method; Compressed air energy storage; Burial depth; Chamber spacing; Chamber group; Closed-form solution

## 1 Introduction

The transition to non-fossil energy power generation faces challenges from uncertainty and instability in energy conversion (Khan & Arsalan, 2016; Gupta, 2016). Integrating energy storage technologies into the grid improves reliability, enables load shifting, and reduces transmission costs (Cheng et al., 2006). Underground compressed air energy storage (U-CAES), with its flexible site selection in artificially excavated chambers, is a promising large-scale storage solution, independent of geological constraints (Jin & Peng, 2017). These chambers are subject to combined stresses from high internal air pressure and external forces, requiring focused research on airtightness and structural stability.

Kim et al. (2012a) and Rutqvist et al. (2012) examined shallow rock chambers, demonstrating feasibility and highlighting risks of tensile stresses leading to cracks and gas leakage. Xia et al. (2023) and X. Liu et al. (2023) investigated crack initiation in lining structures, while Geng et al. (2024) studied operational pressure and temperature variations. CAES chambers in hard rock are commonly designed as tunnel arrays (Zimmels et al., 2002), with bur-

* Corresponding author at: Department of Geotechnical Engineering, College of Civil Engineering, Tongji University, Shanghai 200092, China.
*E-mail address:* zhaocheng@tongji.edu.cn (C. Zhao).
Peer review under the responsibility of Tongji University

https://doi.org/10.1016/j.undsp.2025.03.010
2467-9674/© 2026 Tongji University. Publishing Services by Elsevier B.V. on behalf of KeAi Communications Co. Ltd.
This is an open access article under the CC BY license (http://creativecommons.org/licenses/by/4.0/).

ied depth (Xia et al., 2014, 2016), chamber radius, and spacing (Wang et al., 2020) as critical design factors. However, adjusting burial depth and spacing in pilot projects (Kim et al., 2013, 2016; Jiang et al., 2020) and replicating confining pressure alongside internal air pressure in model experiments (Tunsakul et al., 2014) remain challenging, leading most studies to rely on numerical simulations and limit equilibrium theories of rock uplift.

Research on burial depth for CAES chambers often utilizes the limit equilibrium method, analyzing the uplift of overburden rock under internal pressure (Stille et al., 1994; Brandshaug et al., 2001; Kim et al., 2012b; Xu et al., 2022). The Norwegian Design Code, an empirical approach for water intake tunnel chambers under similar loading, is also a limit equilibrium method but always overly conservative. Variations in failure assumptions exist: Kim et al. (2012b) modeled a linear failure curve for overburden rock to derive burial depth, while Xu et al. (2022) applied a power-function failure curve. Despite differing assumptions, results for safe burial depths are broadly consistent. However, extending failure curves to the surface overestimates burial depths if rock strength is ignored and underestimates them if it is included, leading to arbitrary safety factor selection (Carranza-Torres et al., 2017). Research on CAES chamber spacing is limited and is typically conducted independently of the burial depth study. Wang et al. (2020) analyzed the effect of spacing on the plastic zone in surrounding rock using numerical simulation, while Sun et al. (2024) evaluated stability by assessing whether the plastic zones in rock walls between chambers remain unconnected. The aforementioned studies have established the influence patterns of burial depth, chamber radius, and spacing on stability, laying a foundation for further research.

Abstracting the chamber group model as the problem of an infinite planar plate under external pressure containing multiple circular holes with internal pressure is a research approach that allows simultaneous investigation of the relationships between burial depth, chamber radius, and spacing. The bipolar coordinate method (Ling, 1948; Chen et al., 2009; Liu et al., 2024), Schwarz alternating method (Salerno & Mahoney, 1968; Ukadgaonker, 1980; Mota et al., 2019, Zeng et al., 2023), or conventional complex variable function method (Liu, 1985; Hsieh & Hwu, 2024), are commonly used and relatively accurate, but they require complex series summation or iterative calculations. Numerical simulation methods (Wang et al., 2020; Sun et al., 2024; Ng et al., 2024), which demand high grid resolution or complex iterative computations, are also commonly used. In recent years, many semi-analytical solutions have been developed using swarm optimization algorithms, such as the sparrow search method (Xue & Shen, 2020), particle swarm optimization (Mahdevari & Khodabakhshi, 2021), and the differential evolution algorithm (Chang et al., 2023; Sheng et al., 2024). These methods can solve for stress fields, but they are less effective in developing generalized formulas for safe burial depth and spacing.

Weijermars et al. (2020) proposed a linear superposition method (LSM) capable of providing an analytical expression for the stress field of multiple circular holes in an elastic plate. The closed-form solution foundation of LSM enables superior generalizability, such as incorporating Eulerian time-stepping (Pham & Weijermars, 2020) or combining with other methods (Weijermars, 2022). Nevertheless, the original LSM inadequately addresses issues such as stress redistribution in the central pillar, requiring modifications to adapt it to CAES chamber group scenarios. After completing the elastic stress field calculation, the results can be applied to the plasticity criterion to approximately analyze the distribution of the plastic zone (Liu, 1985).

In this study, the computational logic of the LSM was optimized, and certain superposition terms were corrected for its application to CAES chamber group scenarios, resulting in the modified linear superposition method (M-LSM). Using M-LSM, the elastic stress distribution in the surrounding rock of chambers was obtained, and its patterns under various influencing factors were analyzed. Furthermore, by incorporating the elastic displacement components into the plasticity criterion, the relationships between the minimum safe burial depth and minimum safe chamber spacing, under a criterion for maintaining surrounding rock stability, were derived.

## 2 Complete computational methodology of M-LSM

### *2.1 Fundamental assumptions of the M-LSM for CAES chamber group applications*

The LSM linearly superimposes displacement fields from multi-chamber excavation and internal pressure loading to compute strain and stress tensor fields via compatibility and constitutive equations. To adapt this method for analyzing safe burial depth and chamber spacing in an air storage chamber group, modifications to its fundamental assumptions are required.

#### *2.1.1 Fundamental assumptions for the CAES chamber group and the surrounding rock*

Hard rock CAES chamber groups are typically arranged in linear arrays of tunnel-shaped chambers, aligning with plane strain conditions due to their axial lengths exceeding width and height. Site selection for U-CAES prioritizes safety and sealing, favoring massive, thick rock layers with intact rock masses, minimal joint development, and high integrity. The surrounding rock is assumed to be homogeneous, isotropic, and ideal elastoplastic. This study focuses on the elastoplastic zone of the surrounding rock, excluding excavation-induced damage. This study focuses on advanced adiabatic CAES technology, where chambers under these conditions experience no significant tempera-

ture stresses or thermal damage. Thus, the impact of temperature changes on the surrounding rock is neglected. Unlined or simply lined chambers with an applied sealing layer are assumed, with the lining and sealing layer excluded from load-bearing considerations and their effects therefore neglected.

#### 2.1.2 Modifications to the fundamental assumptions of the original method in M-LSM

In the original LSM, the displacement vector fields induced by excavation and internal pressure were superimposed. However, this superposition resulted in a magnification of the displacement induced by the original in-situ stress, leading to the need for further correction. In the M-LSM proposed in this study, the displacement induced by the initial in-situ stress is separated from excavation-induced displacement to ensure independence between displacement fields. The superimposed displacement components now explicitly include three sequential components: initial in-situ stress, excavation, and air injection, clarifying their physical meaning.

The original LSM includes the following assumptions:

(1) Assumption for the initial in-situ stress components. In the calculation of each displacement component, the surrounding rock is assumed to behave as an infinitely large elastic plate. The self-weight of the rock mass is considered as the initial stress state applied at infinity. Only the self-weight stress in the vertical direction is considered, while the horizontal stress is assumed to be the self-weight stress multiplied by the lateral pressure coefficient.
(2) Assumption for the excavation-induced displacement components. The gravitational changes and shape alterations induced by the excavation of the chamber are neglected.

In the M-LSM proposed in this study, the following corrections are made to the above assumptions:

(1) Correction for the initial in-situ stress components. Since the axis of tunnel-type CAES chambers is typically parallel to the ground, when studying the deformation and stress behavior of the surrounding rock, the initial in-situ stress components are corrected to account for the variation of vertical earth stress with depth and the corresponding change in horizontal stress.
(2) Correction for the air injection displacement components. To more accurately reflect the impact of excavation, the shape changes induced by excavation are considered. These shape alterations affect the stress distribution during pressurization and thus require correction of the air injection displacement components.

Additionally, the effectiveness of these corrections is further analyzed to assess whether they can be neglected.

### 2.2 Refinements of computational logic and result in the original LSM

#### 2.2.1 Components of the displacement field in polar coordinates

The polar coordinate form of the stress components induced by excavation for a single chamber with the chamber center at the origin is given by the Kirsch solution (Timoshenko & Goodier, 1970):

$$\begin{cases} \sigma_\theta = \left[\frac{1}{2}(1+\lambda)\left(1+\frac{r_a^2}{r^2}\right)+\frac{1}{2}(1-\lambda)\left(1+3\frac{r_a^4}{r^4}\right)\cos 2\theta\right]p_0 \\ \sigma_r = \left[\frac{1}{2}(1+\lambda)\left(1-\frac{r_a^2}{r^2}\right)-\frac{1}{2}(1-\lambda)\left(1+3\frac{r_a^4}{r^4}-4\frac{r_a^2}{r^2}\right)\cos 2\theta\right]p_0 \\ \tau_{r\theta} = \left[\frac{1}{2}(1-\lambda)\left(1-3\frac{r_a^4}{r^4}+2\frac{r_a^2}{r^2}\right)\sin 2\theta\right]p_0 \end{cases}, \quad (1)$$

where $p_0$ (MPa) is the vertical earth stress at the depth of the chamber center, $r_a$ (m) is the radius of the chamber, and $\lambda$ is the lateral pressure coefficient. $r$ (m) and $\theta$ (°) represent the polar radius and polar angle, respectively, and $\sigma_\theta$, $\sigma_r$, and $\tau_{r\theta}$ (MPa) represent circumferential stress, radial stress, and shear stress, respectively.

The displacement field can be obtained through the constitutive equations and displacement compatibility equations:

$$\begin{cases} u_r = \frac{1+v}{2E}p_0\left\{(1+\lambda)\left[\frac{r_a^2}{r}-(2v-1)r\right]-(1-\lambda)\left[4(1-v)\frac{r_a^2}{r}-\frac{r_a^4}{r^3}+r\right]\cos 2\theta\right\} \\ u_\theta = \frac{1+v}{2E}p_0\left\{(1-\lambda)\left[2(1-2v)\frac{r_a^2}{r}+\frac{r_a^4}{r^3}+r\right]\sin 2\theta\right\} \end{cases}, \quad (2)$$

where $E$ (MPa) is the deformation modulus, and $v$ is Poisson's ratio.

At this juncture, this displacement includes the displacement under the initial in-situ stress. Let $r_a = 0$ m (indicating the chamber has not been excavated), and calculate the displacement components under the initial in-situ stress, denoted as $u_{r,0}$ and $u_{\theta,0}$:

$$\begin{cases} u_{r,0} = \frac{1+v}{2E}p_0[(1+\lambda)(1-2v)r-(1-\lambda)r\cos 2\theta] \\ u_{\theta,0} = \frac{1+v}{2E}p_0(1-\lambda)r\sin 2\theta \end{cases}. \quad (3)$$

Subsequently, the displacement components induced by excavation can be separated out, denoted as $u_{r,\mathrm{ex}}$ and $u_{\theta,\mathrm{ex}}$:

$$\begin{cases} u_{r,\mathrm{ex}} = \frac{1+v}{2E}p_0\frac{r_a^2}{r}\left\{(1+\lambda)-(1-\lambda)\left[4(1-v)-\frac{r_a^2}{r^2}\right]\cos 2\theta\right\} \\ u_{\theta,\mathrm{ex}} = \frac{1+v}{2E}p_0\frac{r_a^2}{r}\left\{(1-\lambda)\left[2(1-2v)+\frac{r_a^2}{r^2}\right]\sin 2\theta\right\} \end{cases}. \quad (4)$$

The problem of air injection in a circular chamber without considering in-situ stress can be simplified to an infinitely thick-walled cylinder subjected to internal pressure, with the stress components in polar coordinates given by the Lame solution (Timoshenko & Goodier, 1970):

$$\begin{cases} \sigma_{r,\mathrm{in}} = p_a\frac{r_a^2}{r^2} \\ \sigma_{\theta,\mathrm{in}} = -p_a\frac{r_a^2}{r^2} \end{cases}, \quad (5)$$

where $p_a$ (MPa) is the maximum internal air pressure.

Solving for the displacement components, denoted as $u_{r,\mathrm{in}}$ and $u_{\theta,\mathrm{in}}$:

$$\begin{cases} u_{r,\mathrm{in}} = -\frac{1+v}{E} p_{\mathrm{a}} \frac{r_{\mathrm{a}}^2}{r} \\ u_{\theta,\mathrm{in}} = 0 \end{cases}. \tag{6}$$

At the juncture, the displacement components of the displacement fields to be superimposed are obtained in polar coordinates. Figure 1 shows the displacement (vector) of one certain point in the surrounding rock and the stress distribution along the axis ($\theta = 0$, $r \geq r_{\mathrm{a}}$) during initial in-situ stress, excavation, and air injection.

*2.2.2 Transformation to Cartesian coordinates, origin shift, superposition, and solution*

Considering the problem of multi-chamber, for the purpose of superposition, the displacement components in polar coordinates are transformed into Cartesian coordinates, with the $i$-th chamber center located at any coordinate $(x_{\mathrm{a},i}, y_{\mathrm{a},i})$. The displacement components induced by the initial in-situ stress, without the need for an origin shift, can be directly obtained in the Cartesian coordinate system, denoted as $u_{x,0}$ and $u_{y,0}$:

$$\begin{cases} u_{x,0} = \frac{1+v}{E} p_0 (\lambda - \lambda v - v) x \\ u_{y,0} = \frac{1+v}{E} p_0 (1 - v - \lambda v) y \end{cases}, \tag{7}$$

where $x$ (m) and $y$ (m) represent the horizontal and vertical coordinates.

After coordinate transformation and origin shift (these operations are similar to those in Weijermars et al. (2020)), the excavation and air injection displacement components for the $i$-th chamber are as follows:

$$\begin{cases} u_{x,\mathrm{ex},i} = \frac{1+v}{2E} p_0 \frac{r_{\mathrm{a}}^2 (x - x_{\mathrm{a},i})}{(x - x_{\mathrm{a},i})^2 + (y - y_{\mathrm{a},i})^2} \\ \quad \times \left\{ (1+\lambda) + (1-\lambda) \left[ \frac{r_{\mathrm{a}}^2}{(x - x_{\mathrm{a},i})^2 + (x - x_{\mathrm{a},i})^2} + 4(v-1) \right] \frac{(x - x_{\mathrm{a},i})^2 - (y - y_{\mathrm{a},i})^2}{(x - x_{\mathrm{a},i})^2 + (y - y_{\mathrm{a},i})^2} \right\} \\ \quad - \frac{1+v}{2E} p_0 \frac{r_{\mathrm{a}}^2 (y - y_{\mathrm{a},i})}{(x - x_{\mathrm{a},i})^2 + (y - y_{\mathrm{a},i})^2} \\ \quad \times (1-\lambda) \left( \frac{r_{\mathrm{a}}^2}{(x - x_{\mathrm{a},i})^2 + (y - y_{\mathrm{a},i})^2} + 2(1-2v) \right) \frac{2(x - x_{\mathrm{a},i})(y - y_{\mathrm{a},i})}{(x - x_{\mathrm{a},i})^2 + (y - y_{\mathrm{a},i})^2}, \\ u_{y,\mathrm{ex},i} = \frac{1+v}{2E} p_0 \frac{r_{\mathrm{a}}^2 (y - y_{\mathrm{a},i})}{(x - x_{\mathrm{a},i})^2 + (y - y_{\mathrm{a},i})^2} \\ \quad \times \left\{ (1+\lambda) + (1-\lambda) \left[ \frac{r_{\mathrm{a}}^2}{(x - x_{\mathrm{a},i})^2 + (x - x_{\mathrm{a},i})^2} + 4(v-1) \right] \frac{(x - x_{\mathrm{a},i})^2 - (y - y_{\mathrm{a},i})^2}{(x - x_{\mathrm{a},i})^2 + (y - y_{\mathrm{a},i})^2} \right\} \\ \quad - \frac{1+v}{2E} p_0 \frac{r_{\mathrm{a}}^2 (x - x_{\mathrm{a},i})}{(x - x_{\mathrm{a},i})^2 + (y - y_{\mathrm{a},i})^2} \\ \quad \times (1-\lambda) \left( \frac{r_{\mathrm{a}}^2}{(x - x_{\mathrm{a},i})^2 + (y - y_{\mathrm{a},i})^2} + 2(1-2v) \right) \frac{2(x - x_{\mathrm{a},i})(y - y_{\mathrm{a},i})}{(x - x_{\mathrm{a},i})^2 + (y - y_{\mathrm{a},i})^2}, \end{cases} \tag{8}$$

and

$$\begin{cases} u_{x,\mathrm{in},i} = -\frac{(1+v)}{E} p_{\mathrm{a}} \frac{(x - x_{\mathrm{a},i})}{(x - x_{\mathrm{a},i})^2 + (y - y_{\mathrm{a},i})^2} \\ u_{y,\mathrm{in},i} = -\frac{(1+v)}{E} p_{\mathrm{a}} \frac{(y - y_{\mathrm{a},i})}{(x - x_{\mathrm{a},i})^2 + (y - y_{\mathrm{a},i})^2} \end{cases}. \tag{9}$$

When excavation and air injection are performed on $n$ chambers in the chamber group, the complete displacement components $u_{x,\Sigma}$ and $u_{y,\Sigma}$ obtained by superposition:

$$\begin{cases} u_{x,\Sigma} = u_{x,0} + \sum_{i=1}^{n} u_{x,\mathrm{ex},i} + \sum_{i=1}^{n} u_{x,\mathrm{in},i} \\ u_{y,\Sigma} = u_{y,0} + \sum_{i=1}^{n} u_{y,\mathrm{ex},i} + \sum_{i=1}^{n} u_{y,\mathrm{in},i} \end{cases}. \tag{10}$$

When calculating the stress tensor field, the complete displacement components must be used. After obtaining the complete strain components, they are substituted into the constitutive equation for plane strain to calculate the stress components $\sigma_{x,\Sigma}$, $\sigma_{y,\Sigma}$, and $\tau_{y,\Sigma}$:

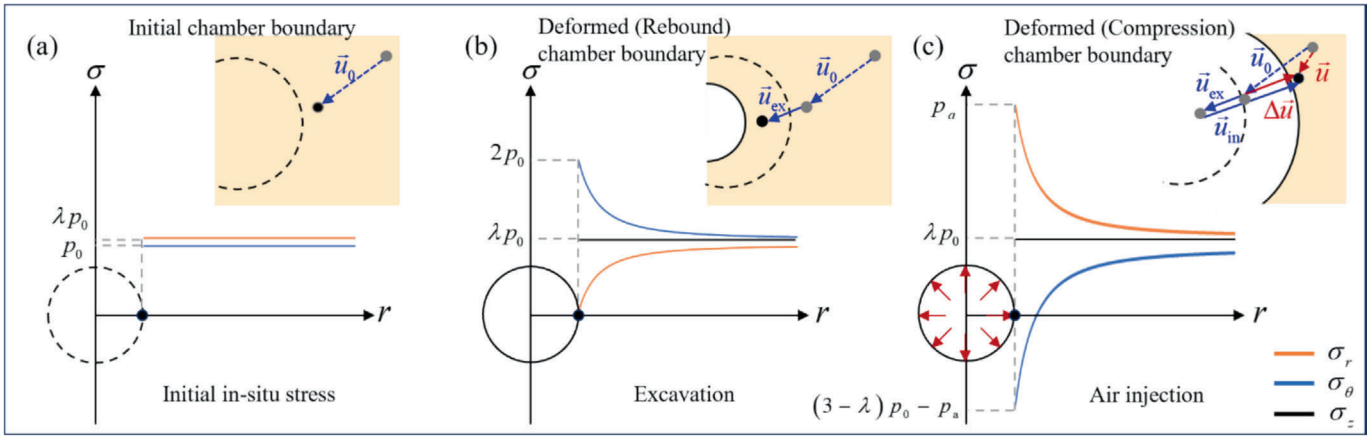


Fig. 1. Displacement vectors and the stress distribution at the chamber sidewall at each stage (a) before chamber excavation, (b) after excavation, and (c) after inflation.

$$\begin{cases} \sigma_{x,\Sigma} = \frac{E}{(1+v)(1-2v)}\left[(1-v)\varepsilon_{x,\Sigma} + v\varepsilon_{y,\Sigma}\right] \\ \sigma_{y,\Sigma} = \frac{E}{(1+v)(1-2v)}\left[v\varepsilon_{x,\Sigma} + (1-v)\varepsilon_{y,\Sigma}\right], \\ \tau_{y,\Sigma} = \frac{E}{2(1+v)}\gamma_{xy,\Sigma} \end{cases} \tag{11}$$

where $\varepsilon_{x,\Sigma} = \frac{\partial u_{x,\Sigma}}{\partial x}$, $\varepsilon_{y,\Sigma} = \frac{\partial u_{y,\Sigma}}{\partial y}$, and $\gamma_{xy,\Sigma} = \frac{\partial u_{x,\Sigma}}{\partial y} + \frac{\partial u_{y,\Sigma}}{\partial x}$ are the complete strain components.

It is worth mentioning that, in the displacement and strain analysis, the focus is on the increment, which is the part of $u_{x,\Sigma}$ and $u_{y,\Sigma}$ after subtracting the contributions from $u_{x,0}$ and $u_{y,0}$.

### *2.3 Corrections of the displacement vector field in the original LSM*

#### *2.3.1 Correction of the displacement vector field induced by initial in-situ stress*

To make the earth stress vary with depth, a correction is applied to the displacement components induced by the in-situ stress. The detailed derivation process is provided in Appendix A.

The displacement components of the in-situ stress compensatory components $u_{x,0}^{\mathrm{com}}$ and $u_{y,0}^{\mathrm{com}}$ are

$$\begin{cases} u_{x,0}^{\mathrm{com}} = -\frac{1+v}{EZ}(\lambda - \lambda v - v)p_0 xy \\ u_{y,0}^{\mathrm{com}} = -\frac{1+v}{2EZ}(1 - \lambda v - v)p_0 y^2 + \frac{1+v}{2EZ}(\lambda - \lambda v - v)p_0 x^2 \end{cases}, \tag{12}$$

where $Z$ (m) is the burial depth of chambers, and the displacement components induced by the corrected in-situ stress $u_{x,0}^{\mathrm{c}}$ and $u_{y,0}^{\mathrm{c}}$ are:

$$\begin{cases} u_{x,0}^{\mathrm{c}} = u_{x,0} + u_{x,0}^{\mathrm{com}} \\ u_{y,0}^{\mathrm{c}} = u_{y,0} + u_{y,0}^{\mathrm{com}} \end{cases}. \tag{13}$$

#### *2.3.2 Correction of the displacement vector field induced by air injection within the central pillar range*

In the adjacent chamber problem, the central pillar exhibits the largest deformation, and the plastic zone typically first appears in this region (This pattern is supported by extensive numerical simulation results in this study); therefore, the stress in this area is of primary concern. Since the displacement superposition method neglects shape changes induced by chamber excavation, a correction is applied to the pressurization displacement components. For ease of description, the surrounding rock is divided into the regions shown in Fig. 2.

As shown in Fig. 3, in polar coordinates, for a single chamber in an infinite plane, the deformation induced by air injection is distributed radially over an infinite region $(r_a, +\infty)$. However, after the excavation of an adjacent chamber, the displacement due to air injection is confined to the range of the central pillar (for example, along the line connecting the chamber centers, displacement is distributed only within $(r_a, S - r_a)$, where $S$ (m) is the spacing between the chamber centers). Therefore, $u_{r,\mathrm{in}}$ and $u_{\theta,\mathrm{in}}$ within the central pillar range need correction.

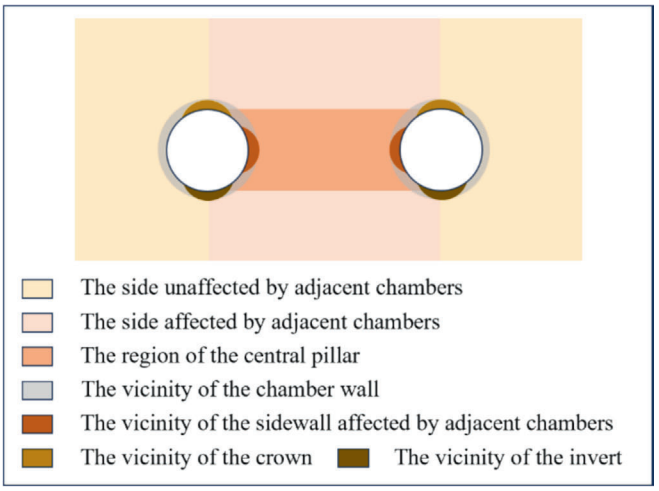


Fig. 2. Rough division of the surrounding rock regions.

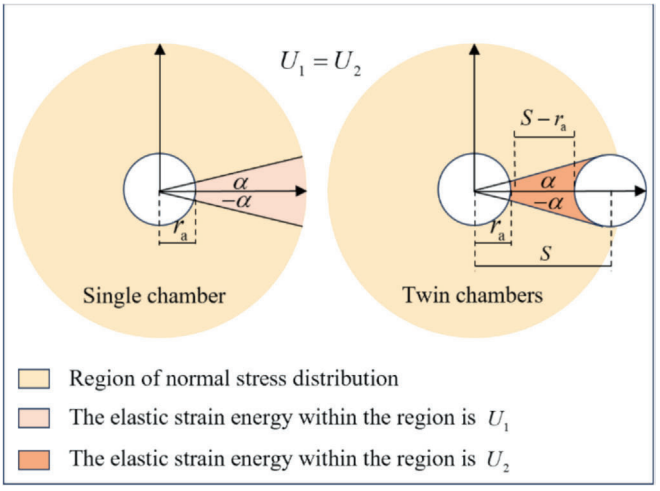


Fig. 3. Deformation and stress redistribution in the range of the central pillar.

Assume that, for a single chamber, the elastic strain energy $U_1$ induced by air injection within the ranges $-\alpha \le \theta \le \alpha$ and $r \ge r_a$ is equivalent to $U_2$ within the central pillar ranges, specifically in $-\alpha \le \theta \le \alpha$ and $r_a \le r \le S - r_a$ (with the right boundary of the central pillar simplified, as the region of primary interest lies along the line connecting the centers of the two chambers). To make the deformation and stress distribution in the central pillar more accurate, the internal pressure $p_{a,1}$ is scaled to $p_{a,2}$. *Here*, $p_{a,1}$ represents the internal air pressure in the single chamber configuration, as well as the actual $p_a$ in the chamber group configuration. In contrast, $p_{a,2}$ is the scaled internal air pressure in the chamber group configuration after correction, reflecting the interaction between the adjacent chambers.

The elastic strain energy density $u$ for plane strain problems in polar coordinates is:

$$u = \frac{1}{2E}\left(\sigma_r^2 + \sigma_\theta^2 + 2v\sigma_r\sigma_\theta\right) + \frac{1+v}{E}\tau_{r\theta}^2. \tag{14}$$

Enter the expression for stress components and integrate them separately within the range to obtain $U_1$ and $U_2$:

$$\begin{cases} U_1 = \int_{-\alpha}^{\alpha}\int_{r_a}^{+\infty}\left[(1+v)\frac{p_{a,1}^2 r_a^4}{E}\frac{1}{r^4}\right]r\mathrm{d}r\mathrm{d}\theta \\ U_2 = \int_{-\alpha}^{\alpha}\int_{r_a}^{s-r_a}\left[(1+v)\frac{p_{a,2}^2 r_a^4}{E}\frac{1}{r^4}\right]r\mathrm{d}r\mathrm{d}\theta \end{cases}. \tag{15}$$

Let $U_1 = U_2$, solve the relationship between $p_{a,1}$ and $p_{a,2}$ as

$$p_{a,2} = \frac{1}{\sqrt{1-\frac{r_a^2}{(S-r_a)^2}}}p_{a,1}. \tag{16}$$

$p_{a,2}$ is greater than $p_{a,1}$, indicating an internal pressure amplification effect due to the presence of an adjacent chamber, with the amplification effect increasing as the spacing decreases. By substituting $p_{a,2}$ for $p_a$ in $u_{r,in}$ and $u_{\theta,in}$, and then superimposing them with the other displacement components, the strain and stress within the central pillar range can be calculated more accurately.

*2.3.3 Effectiveness analysis of the corrections*

In this study, the convergent results of 16 models (with $Z$ of 125, 150, 175 and 200 m and $S$ of 25, 30, 35 and 40 m, a pairwise combination was considered and keeping $r_a$ as 5 m and $p_a$ as 10 MPa) from a finite element analysis tool, ABAQUS, are used as the numerical benchmark for the LSM and M-LSM. All parameters of the corresponding models are kept consistent across the three methods. The surrounding rock parameters are referenced from a CAES project in Suichang, Zhejiang, China (Jiang et al., 2021), as shown in Table 1. The elastic model utilizes elastic parameters, while the elastoplastic model in Section 5.2 incorporates all parameters, where $\gamma$ is the density (kg/m$^3$), $c$ is the cohesion (MPa), and $\varphi$ is the angle of internal friction (°) of the surrounding rock. The detailed modeling process in ABAQUS and the convergence analysis of the results are provided in Appendix B.

The main focus is on $\sigma_y$, i.e., the minimum principal stress $\sigma_3$ at the sidewall of the chamber on the side influenced by the adjacent chamber, as this may indicate a critical tensile stress. Figure 4(a)–(c), taking $Z$ of 150 m and $S$ of 30 m as an example, shows the stress distribution of $\sigma_y$ obtained using ABAUQS ($\sigma_{y,NUM}$), LSM ($\sigma_{y,LSM}$), and M-LSM ($\sigma_{y,M\text{-}LSM}$), respectively. The patterns of the three are similar, but there are differences in the specific values.

Table 1
Surrounding rock physics and mechanics parameters.

| Parameters | $\gamma$ (kg/m$^3$) | $E$ (MPa) | $v$ | $c$ (MPa) | $\varphi$ (°) |
|---|---|---|---|---|---|
| Value | 2900 | 71 600 | 0.24 | 2.5 | 57.0 |

The analysis examines changes in the relative deviation $\delta_1$ before and after applying the correction. $\delta_{1,LSM}$ before correction is calculated as the absolute difference between $\sigma_{y,LSM}$ and $\sigma_{y,NUM}$, divided by $p_0$ the initial in-situ stress at this depth, while $\delta_{1,MLSM}$ after correction is calculated by $\sigma_{y,M\text{-}LSM}$.

Due to the numerous factors influencing stress, the primary factors include $S$, $r_a$, $Z$ ($p_0$), and $p_a$. For ease of analysis, two dimensionless ratios are defined. The spacing-to-radius ratio $\eta = S/r_a$ reflects variations in $S$ and $r_a$. The external-to-internal pressure ratio $\zeta = p_0/p_a$ captures variations in $p_0$ and $p_a$, while also indicating the relative magnitude of $\sigma_y$ at the chamber sidewall. It should be noted that $p_a$ typically satisfies $p_a \geq \max\{\lambda p_0, (3-2\lambda)p_0\}$, in order to ensure the proper sequence of the principal stresses of the sidewall, as shown in Fig. 1(c). Otherwise, the burial depth is excessively deep. This extreme case is not included in this study.

When $\zeta$ exceeds $1/(3-\lambda)$, compressive stress typically dominates at the chamber sidewall, whereas a decreasing ratio leads to the emergence of tensile stress, which increases progressively. Plotting $\delta_1$ as a function of $\eta$ and $\zeta$ in Fig. 4(d) and (e), and smooth it through cubic spline interpolation. The figures offer a clear and intuitive illustration of the impact of key factors on deviation, while the comparison highlights the effectiveness of the correction.

$\delta_{1,LSM}$, as shown in Fig. 4(d), increases as $\eta$ and $\zeta$ decrease. When the central pillar is relatively narrow or $\sigma_y$ at the chamber sidewall is small or negative, $\delta_{1,LSM}$ is large, exceeding 20%. The LSM overestimates $\sigma_y$ compared to numerical simulation results, underestimating the tensile stress, which is less safe.

$\delta_{1,MLSM}$, as is shown in Fig. 4(e), is significantly reduced compared to the uncorrected case. Only under conditions of $\eta < 4$ and $\zeta < 0.5$ does the deviation exceed 10%. Since this condition does not occur in subsequent studies on safe burial depth and spacing, the correction is considered effective and essential in chamber spacing studies.

In summary, the above analysis demonstrates that these corrections effectively address the limitations of the original LSM, providing a more accurate representation of the stress concentrations in chamber groups. This improvement facilitates more reliable research on safe burial depths and chamber spacing in subsequent studies.

## 3 Elastic stress tensor field distribution patterns of CAES chamber groups based on M-LSM

The solution process of the M-LSM method can be programmed in MATLAB to facilitate the calculation of displacement vector field, strain tensor field, and stress tensor field, as well as to generate color contours. CAES chamber groups are typically arranged in arrays of tunnel-shaped chambers. The horizontally arranged twin-chamber model is selected as the main object to analyze the stress distribution patterns, with the case of the multi-

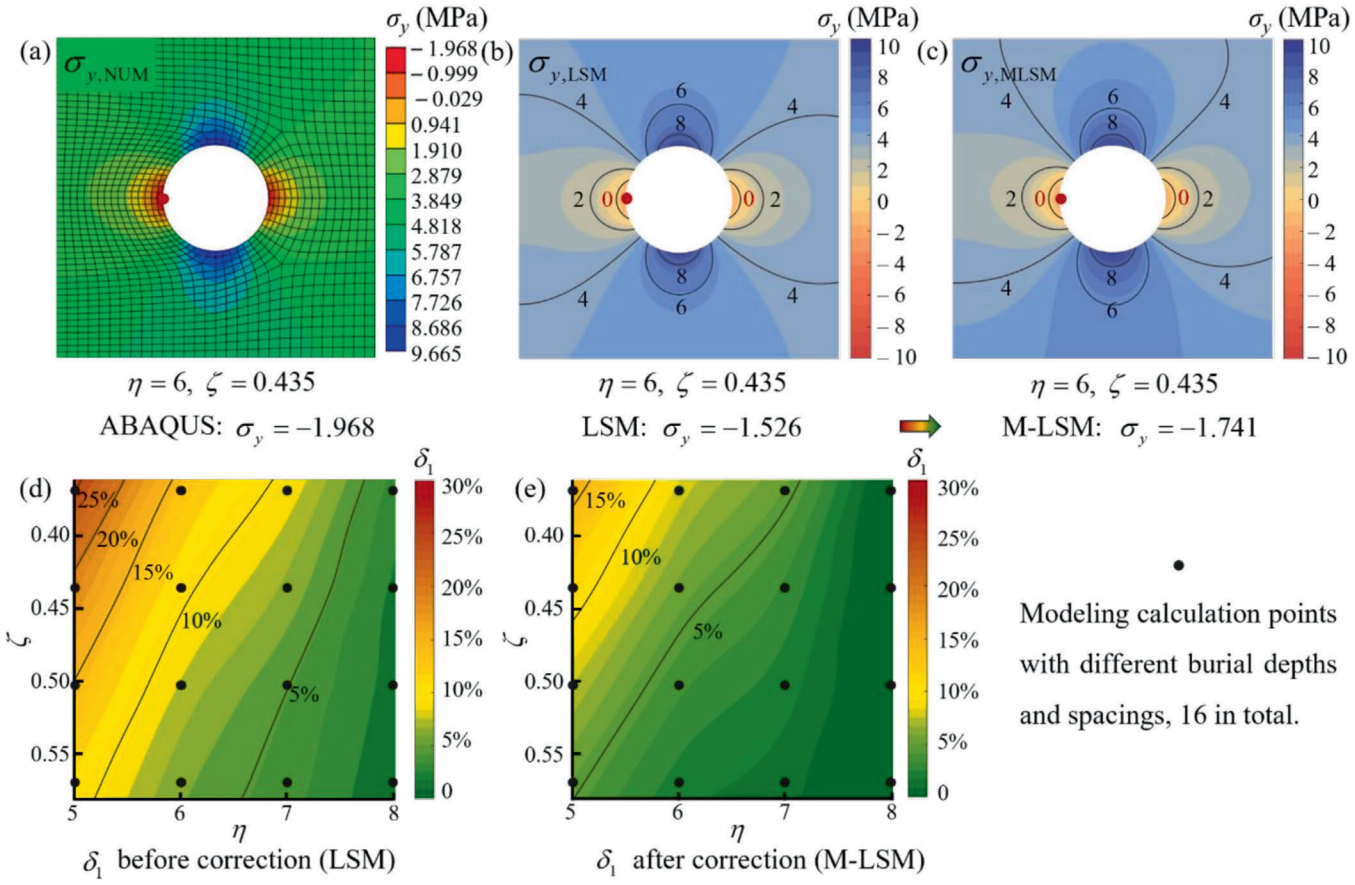


Fig. 4. Color contours of $\sigma_y$ obtained from (a) ABAUQS, (b) LSM, and (c) M-SLM. The relative deviations $\delta_1$ between $\sigma_y$ at the chamber sidewall obtained by LSM and ABAQUS (d) before correction, and (e) after correction (M-LSM).

chamber model analyzed subsequently to verify that the interaction between spaced chambers is negligible.

### *3.1 Variation patterns of stress tensor field in twin-chamber model under different influencing factors*

Table 2 provides a detailed presentation of the stress distribution patterns under the same rock mass conditions, varying with burial depth, spacing, chamber radius, lateral pressure coefficient, and maximum internal pressure. The corresponding color contours are shown in Fig. C1 in Appendix C.

To facilitate the description of the patterns, the surrounding rock is roughly divided into regions, as shown in Fig. 2. When describing the stress directions, circumferential and radial directions are used. This representation takes the center of one chamber as the origin, with the radial direction defined along the radius. This facilitates a more intuitive understanding of the stress directions.

In all the displayed cases, the minimum value of the key stress $\sigma_y$ consistently occurs at the chamber sidewall influenced by the adjacent chamber, indicating the most critical point.

### *3.2 Feasibility assessment of simplifying chamber groups with the twin-chamber model*

Similar to Section 2.3.3, analyze $\sigma_y$ and $\delta_1$ at the sidewall. Suppose there are $n$ ($n \geq 3$) chambers arranged in a row, with a spacing of $S$. According to the M-LSM principle, the distance from the $i$-th chamber to the sidewall of the first chamber is $iS - r_a$, and the superposition amount is $(p_0 - p_{a,2})[r_a/(iS - S - r_a)]^2$, taking the case of $\lambda = 1$ as an example. The error in simplifying chamber groups with the twin-chamber model is $\sum_{i=3}^{n}(p_0 - p_{a,2})[r_a/(iS - S - r_a)]^2$. And the relative error of the twin-chamber model $\delta_{1,twin}$ can be expressed in terms of $\eta$ and $\zeta$ as

$$\delta_{1,twin} = \left|1 - \frac{\eta - 1}{\sqrt{\eta(\eta - 2)}}\frac{1}{\zeta}\right| \sum_{i=2}^{n-1}\left(\frac{1}{i\eta - 1}\right)^2 \leq \frac{1}{\eta^2}\left|1 - \frac{\eta - 1}{\sqrt{\eta(\eta - 2)}}\frac{1}{\zeta}\right|\left(\frac{\pi^2}{6} - 1\right). \quad (17)$$

Table 2
Pattern of stress distribution variation under different influencing factors.

| Influencing factors | Normal stress | Shear stress |
|---|---|---|
| Burial depth | When the burial depth is relatively small, significant circumferential tensile stress and radial compressive stress are observed in the vicinity of the chamber wall. As the burial depth increases, the compressive stress in the surrounding rock increases in all directions, the circumferential tensile stress in the vicinity of the chamber wall decreases until compressive stress appears, and the radial compressive stress further increases. | The shear stress gradually decreases with increasing burial depth. When the burial depth becomes extremely large, which is beyond the scope of this study, the shear stress increases. |
| Chamber spacing | When the chamber spacing is relatively small, the radial compressive stress and circumferential tensile stress within the region of the central pillar are larger compared to other locations. As the chamber spacing increases, the stress concentration gradually decreases, approaching the stress distribution of a single chamber. | When the chamber spacing is relatively small, the shear stress on the side affected by adjacent chambers is lower. As the chamber spacing increases, the shear stress in this area gradually increases until it approaches that on the side unaffected by adjacent chambers. |
| Chamber radius | The increase in chamber radius leads to an increase in circumferential tensile stress and radial compressive stress within the region of the central pillar. However, when both the spacing (20 to 30 m) and radius (5.0 to 7.5 m) increase proportionally, the stress distribution remains virtually unchanged. | An increase in chamber radius leads to an increase in shear stress, with the side unaffected by adjacent chambers experiencing relatively greater shear stress compared to the side affected by adjacent chambers. |
| Maximum internal pressure | When the maximum internal pressure is relatively small, both components within the plane are compressive stresses. As the internal pressure increases, the radial compressive stress in the vicinity of the chamber wall increases, while the circumferential compressive stress decreases until tensile stress appears. | The shear stress increases with the increase in internal pressure. |
| Lateral pressure coefficient | When the lateral pressure coefficient is less than 1, the vicinity of the crown is more prone to tensile stress compared to the vicinity of the sidewall. When the lateral pressure coefficient is greater than 1, the vicinity of the sidewall becomes more prone to tensile stress. | The effect of the lateral pressure coefficient on shear stress is not significant and needs to be analyzed in conjunction with the principal stresses. |

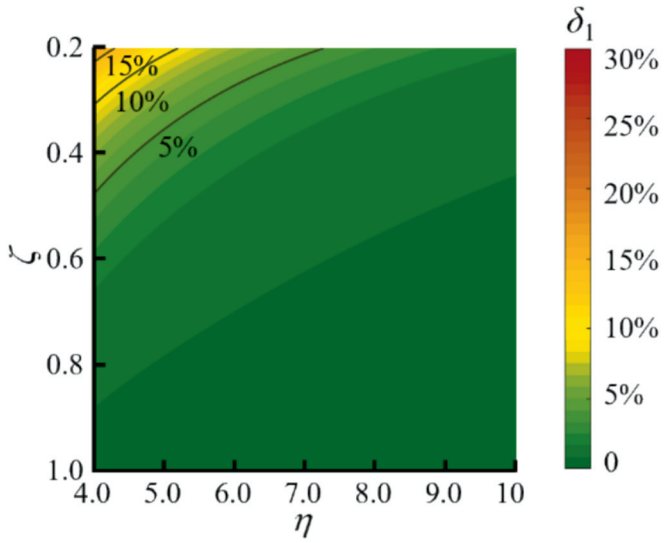


Fig. 5. Relative error $\delta_1$ of the twin-chamber model at the chamber sidewall.

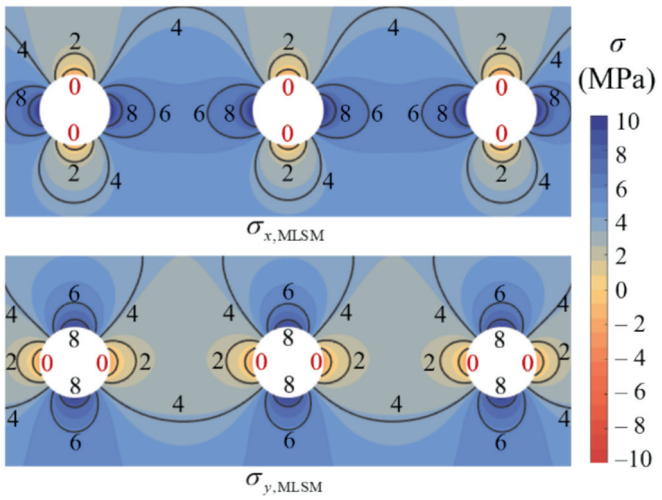


Fig. 6. Color contours of normal stress distribution of the chamber group.

Here, scaling and the conclusion that $\sum_{i=1}^{\infty}\frac{1}{i^2}=\frac{\pi^2}{6}$ are used. The upper limit of $\delta_{1,\mathrm{twin}}$ is plotted in Fig. 5 and can generally be ignored unless $\eta<4$ and $\zeta<0.3$. The conditions of $\lambda\neq1$ are similar.

In addition, the stress distribution pattern of the chamber group under the same parameters, as shown in Fig. 6, is similar to that of the twin chamber in Fig. 4(c). Therefore, simplifying the analysis of multi-chamber cases using the twin-chamber model is feasible.

## 4 Safe burial depth and spacing for CAES chamber groups without plastic zones based on M-LSM

### *4.1 Criterion for safe burial depth and chamber spacing*

In unpressurized structures such as traffic tunnels and mine roadways, plastic zones are commonly used to study

surrounding rock stability. The surrounding rock of a traffic tunnel without internal pressure allows for the formation of a plastic zone while maintaining stability. However, for chambers under cyclic internal pressure, it leads to the accumulation of plastic deformation and exacerbates structural damage (Huang et al., 2021). Experimental studies by Jiang (2024) and J. Liu et al. (2023) on various rock types indicate that under tensile stress, rocks exhibit brittle fracture almost immediately after the elastic limit is reached, with minimal plastic deformation. This rapid brittle failure under tension poses a threat to chamber stability and airtightness. Based on these researches, this study adopts the absence of a plastic zone in the surrounding rock as the stability criterion, which has also been applied by Zhao et al. (2023), Zhang et al. (2024), and Zhao et al. (2025) in studies on the safe burial depth and safe operating pressure of single CAES chambers.

In the study of the safe burial depth and spacing for chamber groups, the M-LSM is used to calculate the elastic stress distribution in the surrounding rock. Then, the Mohr–Coulomb plasticity criterion is applied to approximate the plastic zone in the surrounding rock. If no plastic zone develops in the surrounding rock, the rock is considered safe. When the most dangerous point of stress in the surrounding rock exactly satisfies the plasticity criterion, the corresponding burial depth and spacing are considered the minimum safe burial depth and minimum safe spacing, respectively.

### *4.2 Fundamental assumptions for solving safe burial depth and spacing based on M-LSM*

For the convenience of the study, the following simplifications are made: (1) The twin-chamber model is used as the research object, as the influence of spaced chambers is negligible, which has been confirmed in Section 3.2. (2) During the derivation of the relationship between safe burial depth and spacing, considering that the correction terms for $u_{x,0}^{\mathrm{com}}$ and $u_{y,0}^{\mathrm{com}}$ in the central pillar are less than $r_{\mathrm{a}}/Z$ (typically less than 1/20, and even 0 along the chamber centerline), $u_{x,0}^{\mathrm{com}}$ and $u_{y,0}^{\mathrm{com}}$ can be neglected to simplify equations. (3) $p_0$ is used to replace $Z$, because under the assumption of homogeneous surrounding rock, vertical earth stress is strictly proportional to burial depth (with the proportionality constant being the density $\gamma$). The dimensional units of the replaced term are consistent with the dimensional units of internal air pressure.

At this point, the displacement terms to be superimposed include the displacement terms from the initial in-situ stress, the excavation and air injection displacement terms of each of the two chambers, where the maximum internal pressure is replaced by the modified $p_{\mathrm{a},2}$.

### *4.3 Control equation for safe burial depth and spacing*

After the displacement superposition, the strain and stress can be calculated. It is not difficult to observe that the most dangerous stress point (where the tensile stress is the maximum and the compressive stress is the maximum) is the vicinity of the sidewall adjacent to chambers, i.e., the intersection of the chamber centerline and the chamber boundary. Taking the case of $\lambda = 1$ as an example, the stress components at this point are:

$$\begin{cases} \sigma_x = \left(p_{\mathrm{a},2} - p_0\right)\left[1 + \left(\frac{r_{\mathrm{a}}}{S - r_{\mathrm{a}}}\right)^2\right] + p_0 \\ \sigma_y = -\left(p_{\mathrm{a},2} - p_0\right)\left[1 + \left(\frac{r_{\mathrm{a}}}{S - r_{\mathrm{a}}}\right)^2\right] + p_0 \end{cases}. \tag{18}$$

The stress components at this point are the principal stress, with $\sigma_x$ representing the maximum principal stress $\sigma_1$ and $\sigma_y$ representing $\sigma_3$. If the stress at this point does not reach the plastic state, it represents the limit case where the surrounding rock remains elastic. The stress at this point is then substituted into the Mohr–Coulomb yield criterion as Eq. (19):

$$\sigma_1 = \frac{1 + \sin\varphi}{1 - \sin\varphi}\sigma_3 + \frac{2c\cos\varphi}{1 - \sin\varphi}, \tag{19}$$

where $c$ is the cohesion and $\varphi$ is the internal friction angle.

Substituting $p_{\mathrm{a},2}$ with $p_{\mathrm{a},1}$, the result is

$$9lign\left(\frac{p_{\mathrm{a},1}}{\sqrt{1 - \left(\frac{r_{\mathrm{a}}}{S - r_{\mathrm{a}}}\right)^2}} - p_0\right)\left[1 + \left(\frac{r_{\mathrm{a}}}{S - r_{\mathrm{a}}}\right)^2\right] = p_0\sin\varphi + c\cos\varphi. \tag{20}$$

Let $x = \sqrt{1 - \left(\frac{r_{\mathrm{a}}}{S - r_{\mathrm{a}}}\right)^2}$, and rearrange Eq. (20) into a polynomial form in terms of $x$. At this juncture, $p_0$ represents the minimum safe vertical earth stress in the case of twin-chamber, denoted as $p_{0,2}$, hereafter referred to as the safe burial depth. Meanwhile, $S$ represents the minimum safe spacing, denoted as $S_{\min}$, hereafter referred to as the safe spacing. Therefore, the control equations at this point are

$$\begin{cases} p_{0,2}x^3 - p_{\mathrm{a},1}x^2 - \left[p_{0,2} + (1 + \sin\varphi)p_{0,2} + c\cos\varphi\right]x + 2p_{\mathrm{a},1} = 0 \\ x = \sqrt{1 - \frac{r_{\mathrm{a}}^2}{(S_{\min} - r_{\mathrm{a}})^2}} \end{cases}. \tag{21}$$

### *4.4 Closed-form solutions for safe burial depth and spacing*

There are two scenarios: (1) Given the safe burial depth, solve for the safe spacing. (2) Given the safe spacing, solve for the safe burial depth.

Scenario (1):

In our team's preliminary research, Zhao et al. (2025) provided the safe burial depth range for a single chamber case, where no plastic zone occurs in the surrounding rock. In the case of a single chamber, the minimum safe burial depth can be determined by specifying the maximum internal pressure and the rock mass parameters. The relationship between $p_{a,1}$ and the safe burial depth $p_{0,1}$ for the single chamber case is as Eq. (22):

$$p_{a,1} = \frac{\lambda + 1 - 2|\lambda - 1|}{2}(1 + \sin\varphi)p_{0,1} + c\cos\varphi. \tag{22}$$

Express $p_{0,2}$ in terms of $(1+\delta)p_{0,1}$, where $\delta$ represents the rate of change of burial depth, and substitute it and Eq. (22) into Eq. (21) yields Eq. (23):

$$\begin{aligned}&(1+\delta)p_{0,1}x^3 - \left[(1+\sin\varphi)p_{0,1} + c\cos\varphi\right]x^2\\&-\left[(1+\delta)p_{0,1} + (1+\sin\varphi)(1+\delta)p_{0,1} + c\cos\varphi\right]x\\&+2\left[(1+\sin\varphi)p_{0,1} + c\cos\varphi\right] = 0,\end{aligned} \tag{23}$$

where $x \in (0, 1]$. If Eq. (23) has real roots within this range, the relationship between $S_{\min}$ and $p_{0,1}$ can be further determined.

When $\delta = 0$, $p_{0,2} = p_{0,1}$, Eq. (23) can be simplified to Eq. (24):

$$\begin{aligned}&p_{0,1}x^3 - \left[(1+\sin\varphi)p_{0,1} + c\cos\varphi\right]x^2\\&-\left[(1+\sin\varphi)p_{0,1} + c\cos\varphi + p_{0,1}\right]x\\&+2\left[(1+\sin\varphi)p_{0,1} + c\cos\varphi\right] = 0.\end{aligned} \tag{24}$$

Equation (24) has an obvious real root at $x = 1$, which is also the only real root when $x \in (0, 1]$. When $\delta = 0$, $S_{\min} \to +\infty$, the safe spacing tends to infinity. This indicates that in the twin-chamber problem, if a finite safe spacing exists, the corresponding safe burial depth must be greater than the safe burial depth in the single chamber case under the same conditions. In other words, $\delta$ must satisfy $\delta > 0$, and at this point $x \in (0, 1)$.

This cubic equation can be solved for a given $\delta$. After analysis, the real root of the equation within the range $x \in (0, 1)$ is:

$$x = \frac{-B + \sqrt{T}\left(\cos\frac{\Theta}{3} - \sqrt{3}\sin\frac{\Theta}{3}\right)}{3A}, \tag{25}$$

where

$$\begin{cases} A = (1+\delta)p_{0,1}x^3 \\ B = -\left[(1+\sin\varphi)p_{0,1} + c\cos\varphi\right] \\ C = -\left[(1+\delta)p_{0,1} + (1+\sin\varphi)(1+\delta)p_{0,1} + c\cos\varphi\right] \\ D = 2\left[(1+\sin\varphi)p_{0,1} + c\cos\varphi\right] \\ T = B^2 - 3AC \\ \Theta = \arccos\left[\frac{2TB - 3A(BC - 9AD)}{2T^{\frac{3}{2}}}\right] \end{cases}. \tag{26}$$

The expression for the safe burial depth $p_{0,2}$ for the given $\delta$ is:

$$p_{0,2} = \frac{(1+\delta)\left(p_{a,1} - c\cos\varphi\right)}{1 + \sin\varphi}. \tag{27}$$

Thus, the solution for the safe spacing $S_{\min}$ can be obtained:

$$S_{\min} = r_a\left(1 + \frac{1}{\sqrt{1 - x^2}}\right). \tag{28}$$

Scenario (2):

When the safe spacing $S_{\min}$ is given, $x$ is also simultaneously determined. Thus, the solution for the safe burial depth $p_{0,2}$ can be obtained:

$$p_{0,2} = \frac{(x^2 - 2)p_{a,1} + c\cos\varphi x}{x^3 - (2 + \sin\varphi)x}. \tag{29}$$

Combining the two scenarios above, when either the safe burial depth or the safe spacing is given, the closed-form solution for the other can be obtained.

The complex relationship between the safe spacing and safe burial depth incorporates the influences of the tunnel radius, rock shear strength, and maximum internal pressure. This solution can also be obtained using computational software such as MATLAB under the given parameter conditions. When $\lambda \neq 1$, the control equations for the safe burial depth and safe spacing can also be derived using the same method. In this case, the coefficients of the equation become more complex, and the solution can be obtained using software such as MATLAB.

## 5 Discussion

### *5.1 Variation of safe burial depth and spacing with influencing factors*

Due to the complexity of the solution and the numerous influencing parameters, it is difficult to intuitively analyze its trend. In Section 2.3.3, the spacing-to-radius ratio $\eta$ and the external-to-internal pressure ratio $\zeta$ were defined, with $p_{0,2}$ in $\zeta$ expressed in terms of $p_{a,1}$ and $\delta$, as Eq. (30):

$$\begin{cases} \eta_{\min} = \frac{S_{\min}}{r_a} \\ \zeta_{\min} = \frac{p_{a,1} - c\cos\varphi}{p_{a,1}(1+\sin\varphi)}(1+\delta) \end{cases}. \tag{30}$$

At this juncture, $\eta_{\min}$ can be considered as the minimum safe spacing normalized by the chamber radius, referred to as the relative safe spacing. $\zeta_{\min}$ can be regarded as the minimum safe vertical earth stress normalized by the maximum internal pressure, referred to as the relative safe burial depth. In $\zeta_{\min}$, $\delta$ is the primary variable, which directly reflects the increase in burial depth from the single-chamber safe burial depth $p_{0,1}$, while $p_{a,1}$, $c$, and $\varphi$ are secondary variables, and their values affect the rate of change of burial depth.

Let $\delta$ increase gradually from 0, and plot the relationship between $\eta_{\min}$ and $\zeta_{\min}$ in Fig. 7, where each curve corresponds to a specific set of values for $p_{a,1}$, $c$, and $\varphi$. $p_{a,1}$ takes three different values, while $(c, \varphi)$ are chosen based on the Standard for Engineering Classification of Rock Mass (Ministry of Water Resources of the People's Republic of China, 2014), with values corresponding to good Class I rock (2.5 MPa, 60°), good Class II rock (2.0 MPa, 55°), and poor Class II rock (1.5 MPa, 50°).

When the values of $p_{a,1}$, $c$, and $\varphi$ are given, $\eta_{\min}$ and $\zeta_{\min}$ exhibit an approximate inverse proportional relationship. That is, when the burial depth approaches the single-

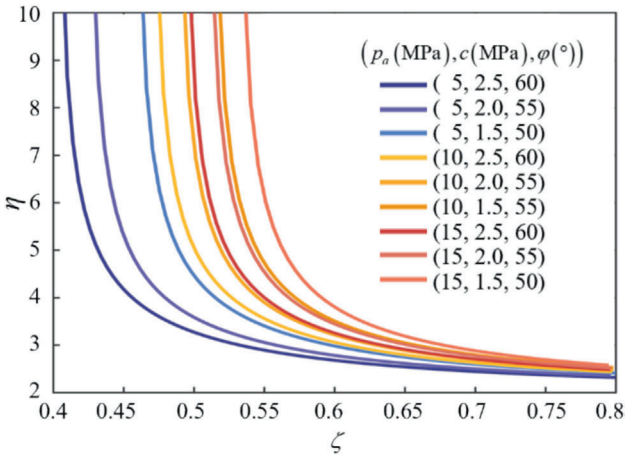


Fig. 7. Relationship between the relative safe burial depth and the relative safe spacing.

chamber safe burial depth, the relative safe spacing tends to infinity; as the relative safe burial depth increases, the relative safe spacing gradually decreases. When the safe burial depth is sufficiently large, the spacing-to-radius ratio approaches 2, indicating that in this condition, the central pillar can be relatively thin. Therefore, when the safe burial depth is close to the single-chamber safe burial depth, a significant reduction in the safe spacing can be achieved with only a small increase in safe burial depth. However, when the burial depth is large enough, the effect of increasing it on reducing the safety spacing becomes less significant.

When $p_{a,1}$ is given, for surrounding rocks with different shear strengths, the following observations can be made as the shear strength increases. (1) For the same (relative) burial depth, the relative safe spacing becomes smaller. (2) For the same relatively safe spacing, the (relative) burial depth becomes smaller. Therefore, rocks with higher shear strength can effectively reduce the safe burial depth ($p_{0,2}$) and spacing. Additionally, rocks with higher shear strength generally possess a higher density, which further contributes to a reduction in the safe burial depth.

When $c$ and $\varphi$ are given, i.e., under the same rock mass conditions, as $p_{a,1}$ increases: (1) For the same relative safe burial depth, the relative safe spacing increases. (2) For the same relative safe spacing, the relative safe burial depth increases. However, considering the increase in $p_{a,1}$, the absolute safe burial depth $p_{0,2}$ will increase to a greater extent. Therefore, when increasing the maximum internal air pressure to enhance storage capacity, careful consideration must be given to the impact of the increased burial depth and spacing on construction costs.

Both reducing the burial depth and decreasing the spacing can enhance the economic viability of the chamber group. By utilizing the analytical relationships between these two factors derived from this study, a target function can be conveniently established, and optimization can be performed.

### *5.2 Comparison of LSM, M-LSM, and numerical modeling method in determining safe burial depth and spacing: a case study of the CAES project in Suichang*

Taking the CAES project in Suichang as an example and using the rock parameters listed in Table 1, with specific values of $p_a = 10$ MPa and $r_a = 5$ m, the following analyses were conducted. First, for burial depths set to 170, 175, and 180 m, the corresponding safe spacings were determined using the LSM, M-LSM, and numerical modeling method, and the resulting deviations were analyzed. Similarly, when the safe spacings are set to 6, 7, and 8 times the radius, the safe burial depths are also calculated.

The determination process using the numerical modeling method is as follows: models, whose materials are set to follow the Mohr–Coulomb plasticity criterion, corresponding to the given burial depths, are established, and the spacing is gradually adjusted until the surrounding rock no longer develops a plastic zone, as shown in Fig. 8(a). Models corresponding to the given spacings and gradually adjusting the burial depth until the surrounding rock no longer develops a plastic zone, as shown in Fig. 8(b).

The safe spacing solutions obtained using the three methods are summarized in Table 3. The safe burial depth solutions are summarized in Table 4. The deviations are based on the numerical modeling method.

The deviations between the LSM and numerical simulation are large, due to LSM underestimating stress concentration in the central pillar, resulting in an overly small calculated safe burial depth and spacing. The burial depth and spacing results based on LSM are mostly unsafe, as evident plastic zones occur in the surrounding rock. In contrast, the deviation between the M-LSM and numerical simulation is small and negligible, highlighting the effectiveness of the modification in M-LSM. However, the numerical simulation requires extensive modeling, trial calculations, and meshes generation to improve accuracy,

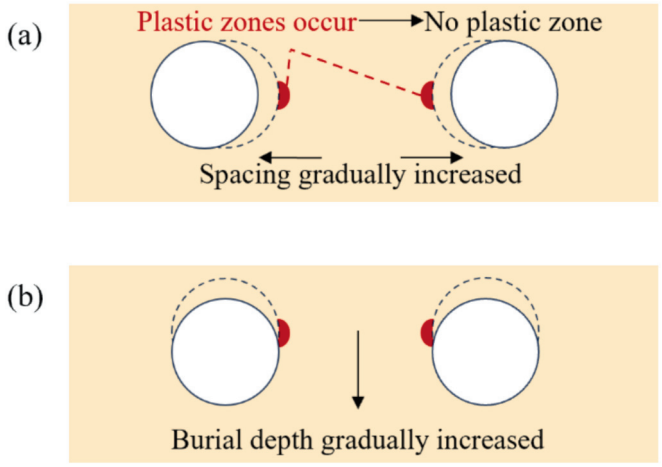


Fig. 8. Numerical simulation methods for determining (a) the minimum safe spacing, and (b) the minimum safe burial depth.

Table 3
Safe spacing determination: comparison of LSM, M-LSM, and ABAQUS.

| Given burial depth (m) | Safe spacing solved by ABAQUS (m) | Safe spacing solved by LSM (relative deviation) | Safe spacing solved by M-LSM (relative deviation) |
|---|---|---|---|
| 170 | 30.4 | 22.2 m (30.0%) | 29.2 m (3.9%) |
| 175 | 25.8 | 18.3 m (29.1%) | 24.2 m (5.4%) |
| 180 | 20.4 | 16.2 m (20.6%) | 21.0 m (2.9%) |

Table 4
Burial depth determination: comparison of LSM, M-LSM, and ABAQUS.

| Given spacing (m) | Safe burial depth solved by ABAQUS (m) | Safe burial depth solved by LSM (relative deviation) | Safe burial depth solved by M-LSM (relative deviation) |
|---|---|---|---|
| 30 | 171.0 | 165.9 m (2.9%) | 169.2 m (1.1%) |
| 35 | 166.0 | 164.7 m (0.7%) | 166.2 m (0.7%) |
| 40 | 163.0 | 164.0 m (0.6%) | 164.2 m (0.7%) |

whereas the mesh-free M-LSM saves computation time and enhances solution accuracy.

### 5.3 Applicability and limitations analysis

The safe criterion, which ensures no plastic zone in the surrounding rock, is applicable to Class I and II surrounding rocks with proper excavation methods and good integrity. Maintaining the elasticity of the surrounding rock can prevent the accumulation of plastic deformation and structural damage, ensuring the long-term stability of chambers under cyclic internal pressure. However, for cases where significant damage has already occurred after excavation, this safe criterion is no longer applicable. In such cases, chambers should be supported, with the new criterion being that the lining, for example, remains undamaged.

In M-LSM, it is important to note that $\sigma_{1,\text{M-LSM}}$ at the sidewall is overestimated. Theoretically, the real $\sigma_{1,\text{real}}$ at this point should be the boundary condition $p_a$, but in M-LSM, it is calculated as in Eq. (31). This overestimation, due to the principle of linear superposition and the modification, is biased towards safety. The method's failure is analyzed based on the relative error $\delta_2 = (\sigma_{1,\text{M-LSM}} - \sigma_{1,\text{real}})/\sigma_{1,\text{real}}$ exceeding 10% tolerance allowed in engineering practice.

Use $\eta$ and $\zeta$ to express $\delta_2$ as shown in Eq. (31) and plot it in Fig. 9.

$$\delta_2 = \frac{1}{\sqrt{1-\left(\frac{1}{\eta-1}\right)^2}} - \left(\frac{1}{\eta-1}\right)^2 \zeta - 1 \tag{31}$$

It is evident that when $\eta \geq 5$, or when $\eta \geq 4$ and $\zeta \geq 0.4$ (for instance, $Z$ is greater than 137.9 m in the case study),

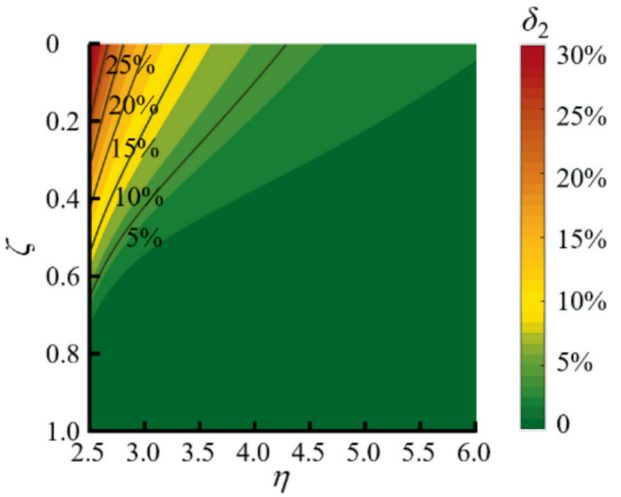


Fig. 9. Relative error $\delta_2$ of $\sigma_1$ at the chamber sidewall in the M-LSM.

$\delta_2$ is consistently less than 10%. When $\eta$ is less than 3, $\delta_2$ always exceeds 10%.

Based on the analysis of $\delta_{1,\text{LSM}}$ in Section 2.3.3, $\delta_{1,\text{twin}}$ in Section 3.2, and $\delta_2$ in this section, define $\zeta < 0.5$ as a shallow burial depth condition and $\eta < 4$ as a small spacing condition. When analyzing the general trend of the elastic stress tensor field distribution using M-LSM, limitations do not need to be considered. However, when solving for the safe burial depth and spacing based on M-LSM, the simultaneous occurrence of the shallow burial depth condition and small spacing condition can lead to errors that cannot be ignored. The error is more sensitive to the small spacing condition, and such a condition should be avoided. Additionally, when $\zeta \geq \max\{\lambda, 3-2\lambda\}$, as an excessively large burial depth condition that typically does not occur, the principal stress sequence needs to be adjusted when calculating the plastic zone. In conclusion, this method can provide high accuracy in most practical application scenarios, but there may be some deviation in extreme cases that require further optimization.

## 6 Conclusions

In this study, the M-LSM was specifically adapted for CAES chamber groups by incorporating corrections for in-situ stress and the central pillar region, optimizing the computational logic of the original LSM, and enhancing the accuracy of the results. Based on M-LSM, the stress distribution patterns in the surrounding rock of chamber groups were obtained, leading to the derivation of the relationship between safe burial depth and spacing under the condition that no plastic zones develop in the surrounding rock. A closed-form solution was achieved. The main conclusions are as follows:

(1) By superimposing the corrected displacement fields of different stages and solving through displacement compatibility equations and constitutive equations,

an analytical expression for the elastic stress distribution in chamber groups can be derived. Compared with the complex variable method, the Schwarz alternating method, and numerical methods, the results are more explicit and intuitive, facilitating trend analysis and application.

(2) The M-LSM can reflect the stress concentration caused by adjacent chamber interactions more accurately: The stress in the central pillar between adjacent chambers shows a redistribution pattern, with tensile stress surpassing the results obtained from direct superposition, suggesting the presence of internal pressure amplification. This amplification effect increases as the spacing decreases. In the case study, the amplification is 0.2 MPa, resulting in a 5% reduction in error compared to the direct superposition method.

(3) The sidewall of the CAES chamber affected by adjacent chambers is typically the area most susceptible to the development of plastic zones. This region warrants particular attention in both research and practical engineering.

(4) In CAES chamber groups, an approximate inverse relationship exists between safe burial depth and spacing. One of these parameters can be determined based on practical requirements, and the other can be calculated using the method proposed in this study. It is recommended that the vertical earth stress at the burial depth be no less than 0.5 times the maximum air internal pressure, and the chamber spacing should be no less than 5 times the radius.

## Data availability

The data that support the findings of this study are available from the corresponding author upon reasonable request.

## CRediT authorship contribution statement

**Zeyuan Sun:** Conceptualization, Methodology, Writing – original draft. **Cheng Zhao:** Supervision, Funding acquisition. **Qinyuan Luo:** Visualization. **Ran Huang:** Validation. **Ning Jia:** Methodology. **Jinquan Xing:** Writing – review & editing. **Jialun Niu:** Software. **Chao Wei:** Software.

## Declaration of competing interest

The authors declare that they have no known competing financial interests or personal relationships that could have appeared to influence the work reported in this paper.

## Acknowledgement

This work was supported by the Special Funds for Science and Technology Supports Carbon Peaking and Carbon Neutrality of the "Science and Technology Innovation Action plan" of Shanghai (Grant No. 22dz1205300), the Interdisciplinary Joint Research Project of Tongji University (Grant No. 2022-3-YB-05), and the Major Science and Technology Projects of China Energy Engineering Corporation Limited 2021 (Grant No. CEEC2021-KJZX-04). The authors are deeply grateful for the support.

## Appendix A Derivation of the correction for displacement vector field induced by in-situ stress

In the fundamental assumptions, the calculation unit is considered a weightless element, while the self-weight of the rock mass is treated as the initial stress state at infinity. This assumption allows the in-situ stress to remain constant, equal to the in-situ stress at the center of the chamber, disregarding its variation with depth. To account for this, a correction is applied to the displacement components induced by the in-situ stress. Using the linear superposition method, the displacement components $u_{x,0}^{\mathrm{com}}$ and $u_{y,0}^{\mathrm{com}}$ of the compensatory components for in-situ stress in the unexcavated and unpressurized state are derived, and superimposed with $u_{x,0}$ and $u_{y,0}$ as the correction components $u_{x,0}^{\mathrm{c}}$ and $u_{y,0}^{\mathrm{c}}$. The depth of the chamber is $Z$, and the in-situ stress at the center of the chamber is calculated as Eq. (A1):

$$\begin{cases} S_{\mathrm{v}} = p_0 \\ S_{\mathrm{h}} = \lambda p_0 \end{cases}. \tag{A1}$$

Compensatory in-situ stress components:

$$\begin{cases} S_{\mathrm{v}}^{\mathrm{com}} = \sigma_y = -\frac{y}{Z} p_0 \\ S_{\mathrm{h}}^{\mathrm{com}} = \sigma_x = -\lambda \frac{y}{Z} p_0 \end{cases}. \tag{A2}$$

Substitute the compensatory components into the constitutive equation:

$$\begin{cases} \varepsilon_x^{\mathrm{com}} = -\frac{1+v}{E} \frac{y}{Z} (\lambda - \lambda v - v) p_0 \\ \varepsilon_y^{\mathrm{com}} = -\frac{1+v}{E} \frac{y}{Z} (1 - \lambda v - v) p_0 \end{cases}. \tag{A3}$$

Substitute into the geometric equation and integrate to obtain the compensatory displacement components:

$$\begin{cases} u_x^{\mathrm{com}} = -\frac{1+v}{EZ} (\lambda - \lambda v - v) p_0 xy + f(y) \\ u_y^{\mathrm{com}} = -\frac{1+v}{2EZ} (1 - \lambda v - v) p_0 y^2 + g(x) \end{cases}, \tag{A4}$$

where $f(y)$ and $g(x)$ are undecomposed univariate functions. Calculate the shear strain of the compensatory components:

$$\gamma_{xy}^{\mathrm{com}} = -\frac{1+v}{EZ} (\lambda - \lambda v - v) p_0 x + f'(y) + g'(x). \tag{A5}$$

The shear strain of the compensatory components is zero, so that Eq. (A5) becomes:

$$-\frac{1+v}{EZ} (\lambda - \lambda v - v) p_0 x + f'(y) + g'(x) = 0. \tag{A6}$$

By comparing functions with the same variables and applying boundary conditions, the undecomposed univariate functions can be obtained:

$$\begin{cases} g(x) = \frac{1+v}{2EZ}(\lambda - \lambda v - v)p_0 x^2 \\ f(y) = 0 \end{cases}. \tag{A7}$$

Therefore, the displacement components of the in-situ stress compensatory components $u_{x,0}^{com}$ and $u_{y,0}^{com}$ are Eq. (12), and the displacement components induced by the corrected in-situ stress $u_{x,0}^{c}$ and $u_{y,0}^{c}$ are Eq. (13). The stress components at a specific point in the surrounding rock before and after correction are shown in Fig. A1.

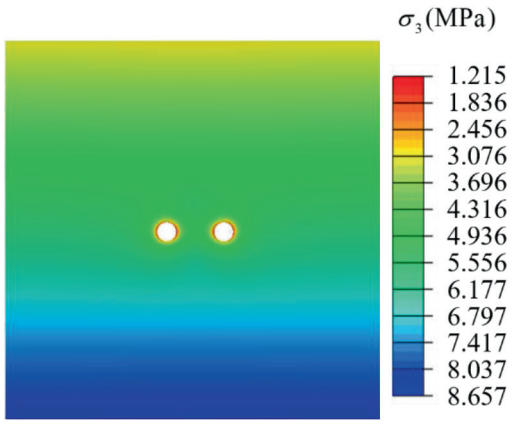


Fig. A1. Stress components at a specific point in the surrounding rock before and after correction.

## Appendix B Numerical benchmark of the M-LSM

The analytical displacement potentials generated by ABAQUS serve as the quantified basis for the M-LSM. ABAQUS is highly applicable to geotechnical and tunnel engineering problems, widely used for its reliable capabilities in solving and analyzing most stress–strain and stability issues related to tunnels and chambers.

In the main text, Section 2.3.3 establishes a set of elastic models as the reference for stress deviation analysis in the M-LSM method, while Section 5.2 establishes a series of elastoplastic models to determine the safe burial depth and spacing. The elastic and elastoplastic models follow the same modeling framework, differing only in their constitutive relations and parameter settings. Furthermore, all models in this study maintain consistent parameters, except for variations in burial depth and spacing. In Section 2.3.3, some of the numerical simulation results for the model with a burial depth of 150 m are presented in Fig. 4(a). To present a more comprehensive set of results within the constraints of space, this appendix provides a thorough description of the modeling process, computational outcomes, and convergence analysis for an elastic model with a burial depth of 200 m and a spacing of 30 m.

The entire model has dimensions of 200 m in both $x$ and $y$ directions. A coordinate system is established with the origin at the center, and two chambers are excavated at coordinates (−15, 0) and (15, 0). Each chamber has a radius of 5 m. The model adopts an elastic constitutive model, with the surrounding rock characterized by a Young's modulus $E$ of 71.6 GPa, a Poisson's ratio $v$ of 0.24, and a unit weight $\gamma$ of 29 kN/m$^3$, the same as those in Table 1. The mechanical boundary conditions are defined as follows: a uniformly distributed load of 2.9 MPa is applied at the top boundary to simulate an additional 100 m depth of burial; the vertical sides restrict horizontal displacement; and the bottom horizontal boundary restricts both horizontal and vertical displacements. The maximum internal air pressure within the chambers is set to 10 MPa. The CPE4 element type, commonly used in tunnel plane strain analysis, is employed, with a finer mesh applied in the vicinity of the chambers. The total number of elements is 19 518, and there are 19 778 nodes in the model. A total of four analysis steps are defined: initial, in-situ stress equilibrium, excavation, and air injection. The lateral pressure coefficient is set as 1 during the in-situ stress equilibrium step.

Convergence was monitored through the data, message, and status files. The analysis proceeded smoothly with no errors or warnings. Each step converged in a single iteration, with the matrix solver performing necessary decompositions and reordering equations to minimize the wavefront. No additional evaluations were required, and there were no numerical issues or discontinuities. The process was stable, and the results indicate reliable convergence and a robust solution. The other numerical calculations in this study have passed the convergence analysis.

Use MATLAB programming to implement the solution process of the M-LSM and generate color contour plots. The plotting area is set to match the ABAQUS model, with all parameters consistent with those input into the ABAQUS model. The color scale of the contours is designed to resemble the rainbow gradient used in ABAQUS post-processing (where positive values indicate tension in ABAQUS, while compression is defined as positive in the M-LSM to align with geomechanical conventions). The color contour results of both methods are compiled in Table B1.

The stress distribution patterns calculated by the M-LSM closely match the results obtained from ABAQUS. In Sections 2.3.3 and 5.3, the deviation of stress calculated by M-LSM has been analyzed and is considered negligible. It is worth noting that finite element calculations typically compute stress as an average value over nodes or elements, so it is difficult to avoid deviations in stress at specific locations. For example, the real value $\sigma_x$ at the chamber wall is 10 MPa, but the finite element results typically show slightly lower values, whereas the M-LSM results tend to be slightly higher. Therefore, it is reliable to use M-LSM to study the stress tensor field distribution patterns, safe burial depth, and safe chamber spacing in air storage chamber groups.

Table B1 Comparison of the results from M-LSM and ABAQUS.

| | M-LSM | Finite element numerical simulation method |
|---|---|---|
| Plotting area / computational model | 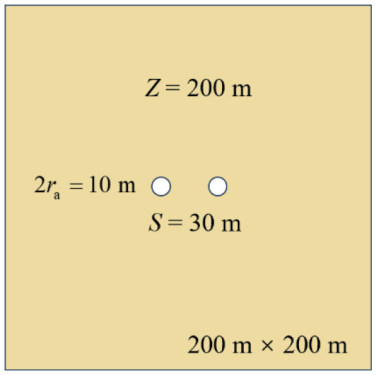 | 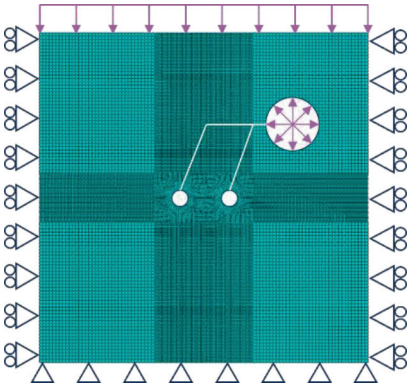 |
| Color contour of $\sigma_x$<br>Unit: MPa | 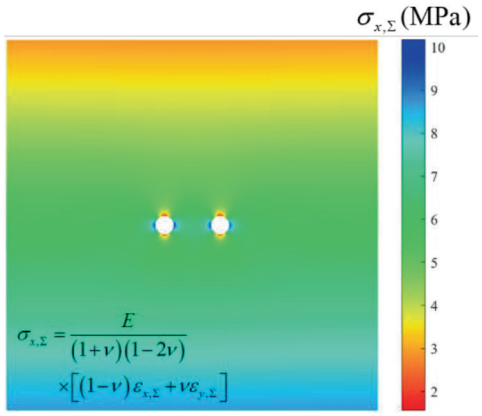 | 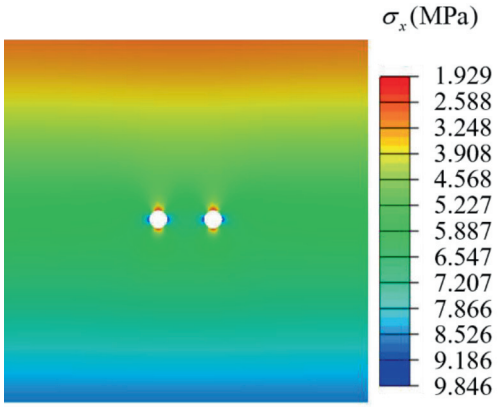 |
| Color contour of $\sigma_y$ | 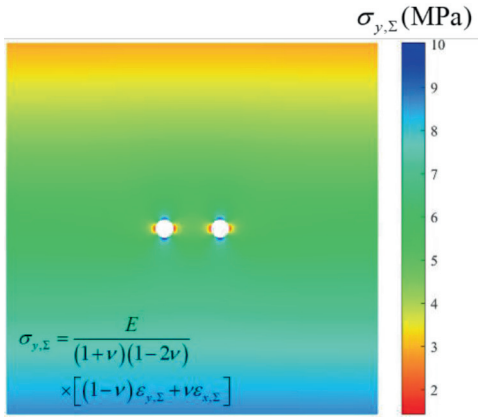 | 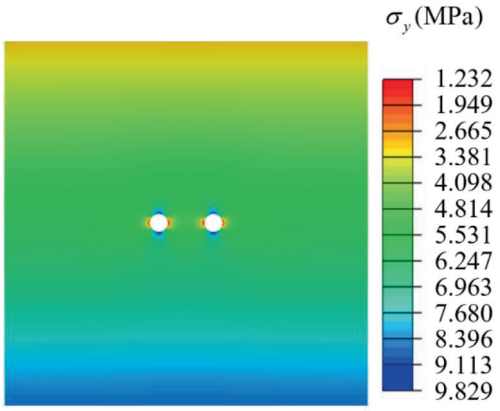 |

Table B1 (*continued*)

| | M-LSM | Finite element numerical simulation method |
|---|---|---|
| Color contour of $\tau_{xy}$ | 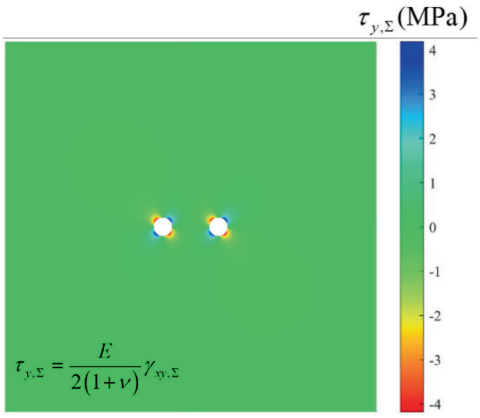 | 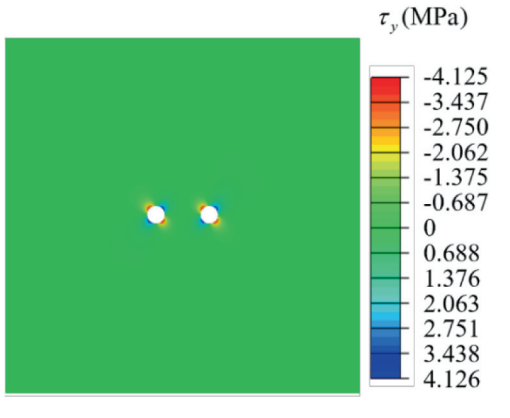 |
| Color contour of $\sigma_1$ ($\sigma_3$ in ABAQUS) | 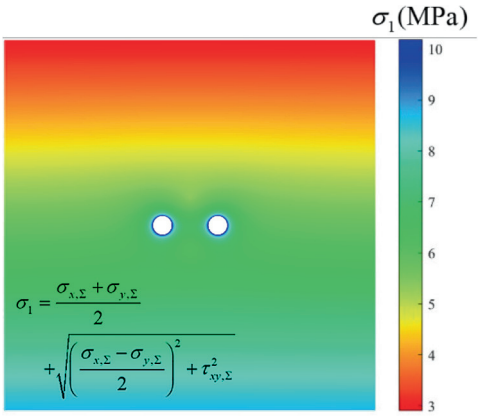 | 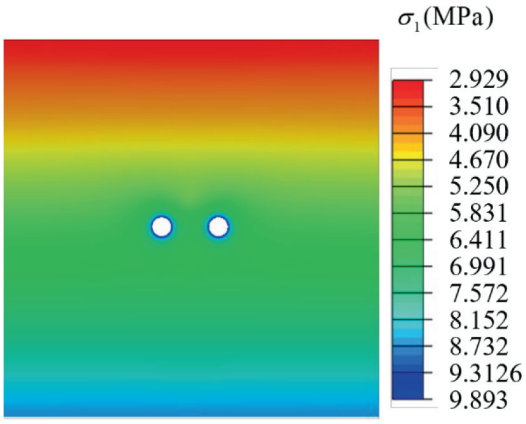 |
| Color contour of $\sigma_3$ ($\sigma_1$ in ABAQUS) | 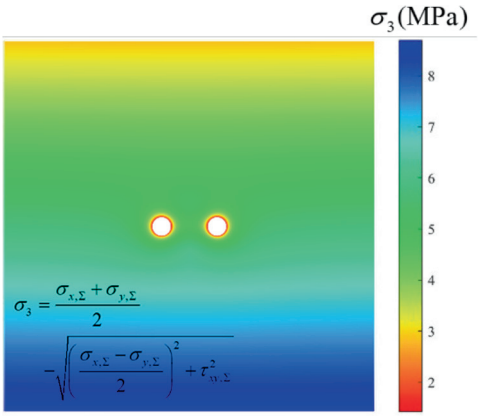 | 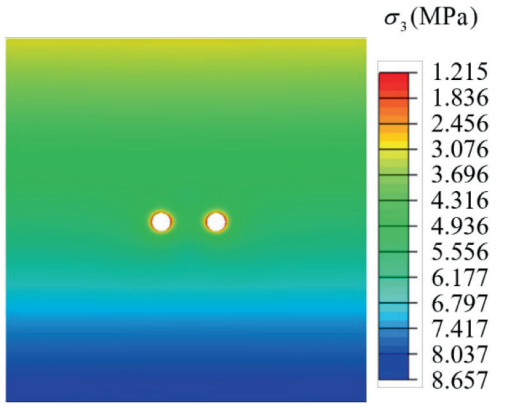 |

## Appendix C Complete results of the variation patterns in elastic stress distribution of chamber groups under different influencing factors

Taking the surrounding rock with parameters in Table 1, stress distribution color contours, as shown in Figs. C1 and C2, were generated for varying burial depths, chamber spacings, chamber radii, maximum internal pressures, and lateral pressure coefficients.

In these color contours, the color scale is set to correspond to stress values: red indicates tensile stress, and blue indicates compressive stress, with deeper shades of red (or blue) representing larger values of tensile (or compressive) stress.

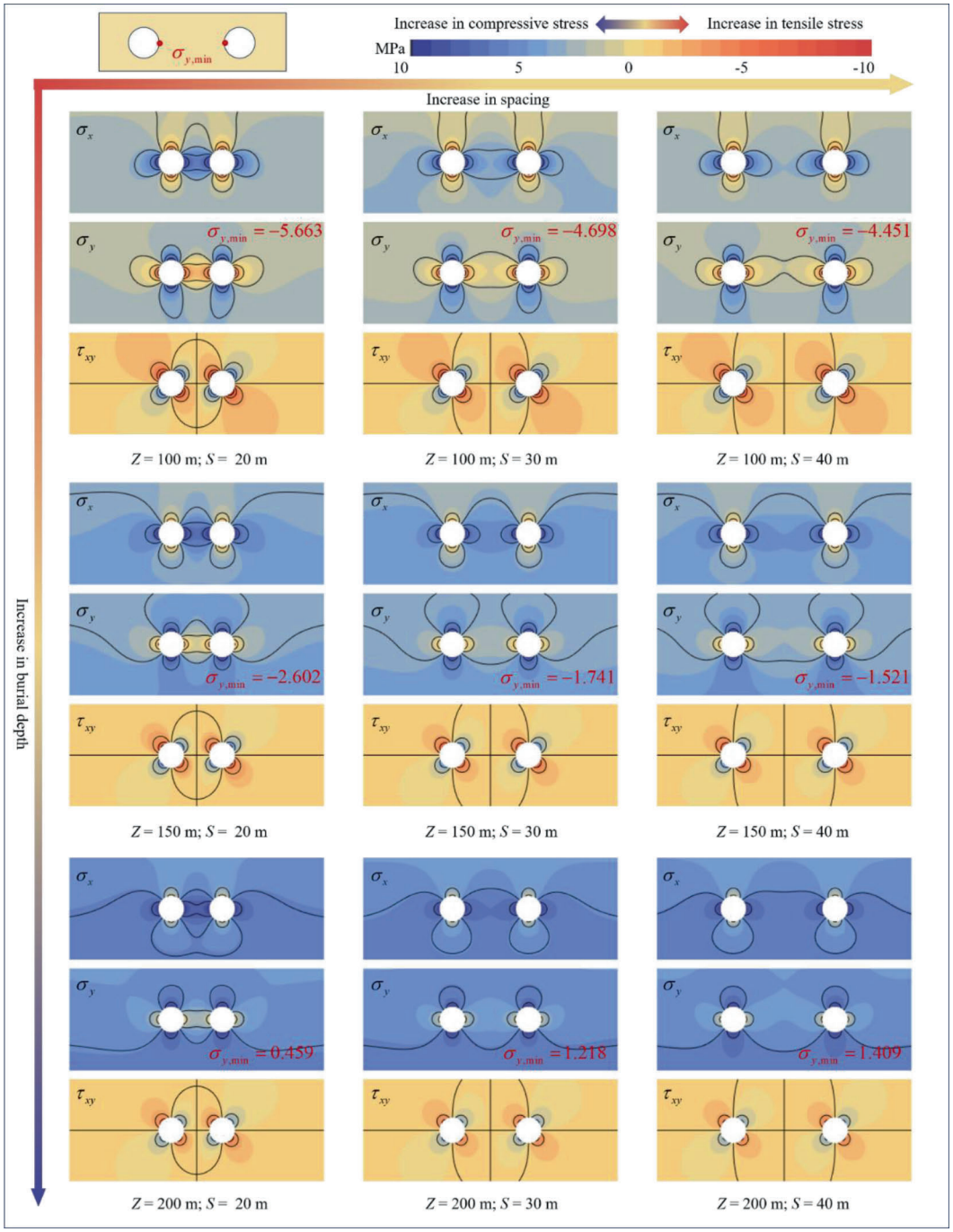


Fig. C1. Color contours of stress components in the surrounding rock under varying burial depths and chamber spacings. The plotting area is set to 100 m × 40 m, with a fixed chamber radius of 5 m, an internal pressure of 10 MPa, and a lateral pressure coefficient of 1.

The deepest red corresponds to a tensile stress of 10 MPa, and the deepest blue corresponds to a compressive stress of 10 MPa. Therefore, the color changes in the color contour corresponding to different parameters can visually reflect the variation in stress distribution. The black contour lines are set at intervals of 2 MPa, with more contour lines indicating a larger gradient of stress variation. In all the displayed cases, the minimum value of the key stress $\sigma_y$ consistently occurs at the sidewall influenced by the adjacent chamber, and is labeled as $\sigma_{y,\min}$ in the figures.

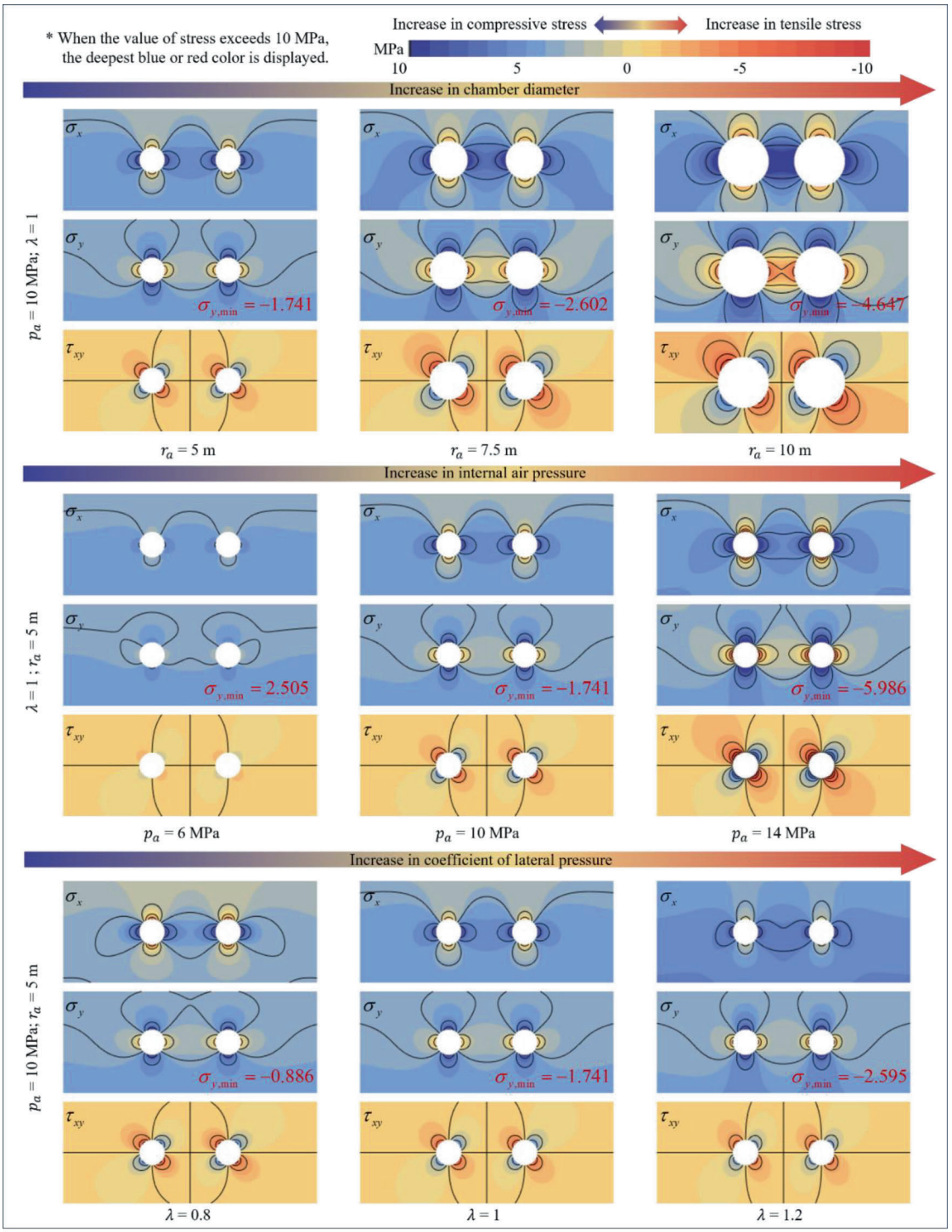


Fig. C2. Color contours of stress components under varying chamber radii, maximum internal pressures, and lateral pressure coefficients. The plotting area is set to 100 m × 40 m, with a fixed burial depth of 150 m and chamber spacing of 30 m. Only one factor is changed in each set of calculations.

## References


Brændshaug, T., Christianson, M., & Damjanac, B. (2001). *Technical Review of the Lined Rock Cavern (LRC) Concept and Design Methodology: Mechanical Response of Rock Mass.* U.S. Department of Energy, National Energy Technology Laboratory. Contract No. DE-AM26-99FT40463.

Carranza-Torres, C., Fosnacht, D., & Hudak, G. (2017). Geomechanical analysis of the stability conditions of shallow cavities for Compressed Air Energy Storage (CAES) applications. *Geomechanics and Geophysics for Geo-Energy and Geo-Resources, 3*(2), 131–174.

Chang, X., Wang, H., & Zhang, Y. (2023). Back analysis of rock mass parameters in tunnel engineering using machine learning techniques. *Computers and Geotechnics, 163*, 105738.

Chen, J.-T., Hsiao, J.-C., & Liou, J.-C. (2009). Bipolar coordinates, image method and the method of fundamental solutions for Green's functions of Laplace problems containing circular boundaries. *International Journal for Computational Methods in Engineering Science and Mechanics, 11*(4), 95–110.

Cheng, S., Yu, W., Wen, J., Sun, H., & Wang, H. (2006). Energy storage technology and its application in power system stability control. *Power System Technology, 30*(10), 1–6 (in Chinese).

Geng, X., Sun, G., Wu, K., Yao, Y., Ji, W., Yu, X., & Wang, J. (2024). Thermodynamic analysis of lined rock caverns for initial inflation and cyclic operational conditions in compressed air energy storage. *Journal of Energy Storage, 99*, 113253.

Gupta, N. (2016). A review on the inclusion of wind generation in power system studies. *Renewable and Sustainable Energy Reviews, 59*, 530–543.

Hsieh, M.-L., & Hwu, C. (2024). Green's functions for anisotropic elastic plates containing polygonal holes. *International Journal of Mechanical Sciences, 276*, 109396.

Huang, F., Zhou, Y., Peng, Y., Gao, X., & Lin, Z. (2021). Study on the strength and deformation characteristics of granite under cyclic loading. *Chinese Journal of Underground Space and Engineering, 17*(2), 356–364 (in Chinese).

Jiang, W. (2024) *Comparative study on rocks in different tensile and compressive tests* [Master's thesis, Nanjing University]. (in Chinese).

Jiang, Z., Li, P., Tang, D., Zhao, H., & Li, Y. (2020). Experimental and numerical investigations of small-scale lined rock cavern at shallow depth for compressed air energy storage. *Rock Mechanics and Rock Engineering, 53*(6), 2671–2683.

Jiang, Z., Li, X., Wang, F., & Ouyang, Y. (2021). Numerical study on stress and deformation characteristics of structure of underground gas storage for CAES in Suichang. *Journal of Changsha University of Science & Technology (Natural Science), 18*(3), 79–86.

Jin, W., & Peng, Y. (2017). Underground gas storage cavern location method for compressed air energy storage engineering in hard rock Area. *Power and Energy, 38*(1), 63–67 (in Chinese).

Khan, J., & Arsalan, M. H. (2016). Solar power technologies for sustainable electricity generation – A review. *Renewable and Sustainable Energy Reviews, 55*, 414–425.

Kim, H.-M., Rutqvist, J., Ryu, D.-W., Sunwoo, C., & Song, W.-K. (2012a). Exploring the concept of compressed air energy storage (CAES) in lined rock caverns at shallow depth: A modeling study of air tightness and energy balance. *Applied Energy, 92*, 653–667.

Kim, H.-M., Park, D.-H., Ryu, D.-W., & Song, W.-K. (2012b). Parametric sensitivity analysis of ground uplift above pressurized underground rock caverns. *Engineering Geology, 135–136*, 86–95.

Kim, H.-M., Rutqvist, J., Jeong, J.-H., Choi, B.-H., Ryu, D.-W., & Song, W.-K. (2013). Characterizing excavation damaged zone and stability of pressurized lined rock caverns for underground compressed air energy storage. *Rock Mechanics and Rock Engineering, 46*(3), 487–504.

Kim, H.-M., Rutqvist, J., Kim, H., Park, D., Ryu, D.-W., & Park, E.-S. (2016). Failure monitoring and leakage detection for underground storage of compressed air energy in lined rock caverns. *Rock Mechanics and Rock Engineering, 49*(1), 573–584.

Ling, C.-B. (1948). On the stresses in a plate containing two circular holes. *Journal of Applied Physics, 19*(1), 77–83.

Liu, J., Liang, C., Wang, L., Pei, J., Dai, J., Lu, G., Zhou, L., & Lin, H. (2023a). Rock tensile testing and problem analysis based on a universal direct tensile method. *Chinese Journal of Rock Mechanics and Engineering, 42*(9), 2140–2147 (in Chinese).

Liu, X., & Hou, X. (1985). Stress analysis for parallel circular tunnels. *Journal of Tongji University (Natural Science), 3*, 15–27 (in Chinese).

Liu, X., Yang, J., Yang, C., Zhang, Z., & Chen, W. (2023b). Numerical simulation on cavern support of compressed air energy storage considering thermo-mechanical coupling effect. *Energy, 280*, 127352.

Liu, Y., Zhang, G., Wang, Z., Li, H., Zhang, H., & Liu, K. (2024). Bipolar coordinate solution of pillar stability for salt cavern energy storage. *Computers and Geotechnics, 173*, 106506.

Mahdevari, S., & Khodabakhshi, M. B. (2021). A hybrid PSO-ANFIS model for predicting unstable zones in underground roadways. *Tunnelling and Underground Space Technology, 117*, 104167.

Ministry of Water Resources of the People's Republic of China (2014). *Standard for engineering classification of rock mass (GB/T 50218—2014)*. Beijing: Standards Press of China (in Chinese).

Mota, A., Tezaur, I., & Alleman, C. (2019). Corrigendum to "the Schwarz alternating method in solid mechanics" [Comput. Methods Appl. Mech. Engrg. 319 (2017) 19–51]. *Computer Methods in Applied Mechanics and Engineering, 344*, 1147–1148.

Ng, C. W. W., Wong, A. Y. Y., Buenaventura, A. D. F., & Zhu, P. Y. (2024). Three-dimensional numerical analysis of twin tunnelling in two-layered soil strata. *Tunnelling and Underground Space Technology, 153*, 106028.

Pham, T., & Weijermars, R. (2020). Hydraulic fracture propagation in a poro-elastic medium with time-dependent injection schedule using the time-stepped linear superposition method (TLSM). *Energies, 13*(24), 6474.

Rutqvist, J., Kim, H.-M., Ryu, D.-W., Synn, J.-H., & Song, W.-K. (2012). Modeling of coupled thermodynamic and geomechanical performance of underground compressed air energy storage in lined rock caverns. *International Journal of Rock Mechanics and Mining Sciences, 52*, 71–81.

Salerno, V. L., & Mahoney, J. B. (1968). Stress solution for an infinite plate containing two arbitrary circular holes under equal biaxial stresses. *Journal of Engineering for Industry, 90*(4), 656–662.

Sheng, Y., Li, P., Yang, S., & Zou, J. (2024). Elastoplastic solutions for deep-buried twin tunnels with arbitrary shapes and various arrangements under biaxial in-situ stress field based on Mohr-Coulomb and generalized Hoek-Brown criteria. *Computers and Geotechnics, 165*, 105896.

Stille, H., Johansson, J., & Sturk, R. (1994). High pressure storage of gas in lined shallow rock caverns—Results from field tests. In *SPE/ISRM Rock Mechanics in Petroleum Engineering* (Paper No. SPE-28115-MS). Society of Petroleum Engineers.

Sun, Z., Zhao, C., Qian, Y., Xing, J., & Niu, J. (2024). Cavern spacing of CAES cavern group in hard rock based on plastic zone and deformation analysis. *IOP Conference Series: Earth and Environmental Science, 1387*(1), 012038.

Timoshenko, S. P., & Goodier, J. N. (1970). Theory of elasticity (3rd ed.). McGraw-Hill, 58–60, 78–84.

Tunsakul, J., Jongpradist, P., Soparat, P., Kongkitkul, W., & Nanakorn, P. (2014). Analysis of fracture propagation in a rock mass surrounding a tunnel under high internal pressure by the element-free Galerkin method. *Computers and Geotechnics, 55*, 78–90.

Ukadgaonker, V. G. (1980). Stress analysis of a plate containing two circular holes having tangential stresses. *AIAA Journal, 18*(1), 125–128.

Wang, Q., Zhang, B., Wang, H., Li, Y., Hu, Z., & Lang, B. (2020). Optimization and stability analysis of layout parameters of lined high-pressure gas storage caverns. *Journal of Engineering Geology, 28*(5), 1123–1131 (in Chinese).

Weijermars, R., Pham, T., & Ettehad, M. (2020). Linear superposition method (LSM) for solving stress tensor fields and displacement vector fields: Application to multiple pressure-loaded circular holes in an elastic plate with far-field stress. *Applied Mathematics and Computation, 381*, 125234.

Weijermars, R. (2022). Production rate of multi-fractured wells modeled with Gaussian pressure transients. *Journal of Petroleum Science and Engineering, 210*, 110027.

Xia, C., Zhang, P., Zhou, S., Zhou, Y., & Wang, R. (2014). Stability and strain analysis of large-scale compressed air energy storage caverns. *Rock and Soil Mechanics, 35*(5), 1391–1398 (in Chinese).

Xia, C., Zhao, H., Mei, S., Zhou, S., Zhang, P., & Zhou, Y. (2016). Quantitative analysis of the influence of burial depth on the stability of compressed air energy storage lined caverns. *Journal of Shaoxing University, 36*(4), 45–51 (in Chinese).

Xia, C., Xu, Y., Zhou, S., Qin, S., & He, X. (2023). Fracture initiation and propagation in the lined underground caverns for compressed air energy storage: Coupled thermo-mechanical phase-field modeling. *Computers and Geotechnics, 157*, 105329.

Xu, Y., Xia, C., Zhou, S., Zhao, H., & Xue, X. (2022). Anti-uplift failure criterion of caverns for compressed air energy storage based on the upper bound theorem of limit analysis. *Chinese Journal of Rock Mechanics and Engineering, 41*(10), 1971–1980 (in Chinese).

Xue, J., & Shen, B. (2020). A novel swarm intelligence optimization approach: Sparrow search algorithm. *Systems Science & Control Engineering, 8*(1), 22–34.

Zeng, G. S., Wang, H. N., & Jiang, M. J. (2023). Analytical stress and displacement of twin noncircular tunnels in elastic semi-infinite ground. *Computers and Geotechnics, 160*, 105520.

Zhang, G., Wang, X., Ke, H., Xiang, Y., Guo, H., Xiong, F., & Hua, D. (2024). Method for determining the operating pressure range of lined underground gas storage caverns for compressed air energy storage. *Chinese Journal of Rock Mechanics and Engineering, 43*(3), 512–520 (in Chinese).

Zhao, C., Sun, Z., Luo, Q., Qian, Y., Niu, J., Wei, C., & Xing, J. (2025). Research on a closed-form solution for safe burial depth range (SDB-RS) of hard rock compressed air energy storage chambers based on no plastic zone criterion. *Geomechanics and Geophysics for Geo-energy and Geo-resources, 11*(1), 48.

Zhao, C., Sun, Z., Qian, Y., Xing, J., Chen, Y., & Niu, J. (2023). *Method for designing the layout of a group of underground compressed air energy storage caverns in hard rock* (Chinese Patent No. CN202310850441.X). CN116992529A (in Chinese).

Zimmels, Y., Kirzhner, F., & Krasovitski, B. (2002). Design criteria for compressed air storage in hard rock. *Journal of Energy Resources Technology, 124*(3), 182–190.